Structures 47 (2023) 1295–1322

Contents lists available at ScienceDirect

Structures

journal homepage: www.elsevier.com/locate/structures

Development of adjustable fluid damper device for the bridges subjected to traffic loads

Hengameh Farahpour [a], Farzad Hejazi [a,b,*]

[a] Department of Civil Engineering, University Putra Malaysia, Malaysia
[b] Faculty of Environment and Technology, The University of The West England, Bristol, United Kingdom

ARTICLE INFO

Keywords:
Seismic excitation
Viscous fluid damper
Bridges
Structural dynamic
Computational fluid dynamic
Dynamic loads
Hydraulic circuit
Semi-active control

ABSTRACT

In this research, an Adjustable Bypass Fluid Damper (ABFD) is developed by utilizing a pair of external fluid flow pipes and flow control valves. The flow control valves control the flow pressure of the fluid passing through bypass pipes and adjusted the function of the fluid damper to limit the displacement of the structure within the allowable range. Therefore, the function of the fluid damper device is adjustable according to the displacement of the structure.

The ABFD device is developed through implementing an adjustable valve in bypass pipes that able to change and adjust the flow and pressure of the oil inside the viscous damper during movement of piston under applied vibrations and control the resultant damping and resistance force of the damper device. Therefore, through the new proposed design, the action of viscous damper has been changed from passive control device to an adjustable system which is capable to function as an device with different capacities and also able to change the response from a damping device to a restrainer system. The analytical model of the proposed ABFD device is developed and the performance of the device has been formulated according to the control valve position. Then the finite volume model of the moving fluid inside the device has been developed and the function of the device was evaluated through Computational Fluid Dynamics analysis.

In the next step, the prototype of ABFD has been fabricated and experimental tests have been conducted using a dynamic actuator to evaluate the performance of the device in various control valve conditions.

The numerical analysis and experimental test results for the ABFD prototype revealed that the developed device is capable of developing a wide range of damping levels and there is a desirable agreement between numerical predictions and experimental results.

Thereafter, to examine the effect of the application of the ABFD device in the bridge structures, the proposed ABFD device was implemented in the 19/5 California overcrossing bridge. The considered bridge equipped with an ABFD device is modeled using the finite element method and it's subjected to the passing vehicle loadings. The results showed that the bridge's response is dramatically improved with the implementation of the six ABFD dampers and the peak displacement of the structure reduces by 35 percent while the control valves are half-open.

1. Introduction

Structural damages are mostly resulted from underestimating displacements and the large dynamic forces applied to the structure during their life spans [25]. Conclusive evidence shows highway bridges are routinely subjected to larger than anticipated vehicle loads so that vibration issues may shorten the useful service life of these vital structures [30]. Given the abundance of bridge failures, many research programs were conducted to improve the dynamic behavior of structures. Full-scale tests and analytical evaluations on a twin 170 m long steel railway bridge were utilized to assess (i) the operational life of the critical detail, (ii) critical spots along the cross beam, and (iii) strain redistribution along with the riveted element during crack grow (Elisa [1]. In this study, the importance of the effective operational life of critical components, elements, parts, connections, or joints was highlighted. The function of critical details of the structure is more sensitive since they are more vulnerable to damage during operation. These components or parts are considered critical points whose functions of them are vital for the stability of structure or performance of the device and it is expected that they are the first elements to experience damage

* Corresponding author.
E-mail address: farzad.hejazi@uwe.ac.uk (F. Hejazi).

https://doi.org/10.1016/j.istruc.2022.11.136
Received 17 June 2022; Received in revised form 28 November 2022; Accepted 28 November 2022

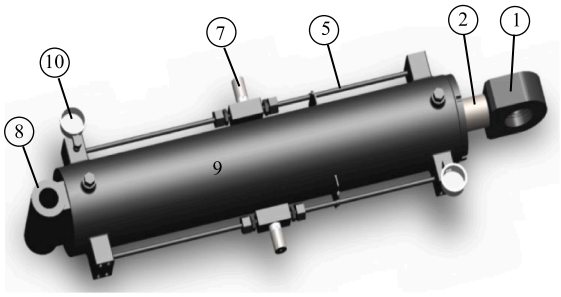

No.	Component
1	Piston Shaft Connector
2	Piston Shaft
3	Piston Head
4	Left Chamber of the Hydraulic Cylinder
5	Bypass Pipes
6	Right Chamber of the Hydraulic Cylinder
7	Flow Control Valves
8	Hydraulic Cylinder Connector
9	Hydraulic Cylinder
10	Pressure Transducer

(a) Assembled view

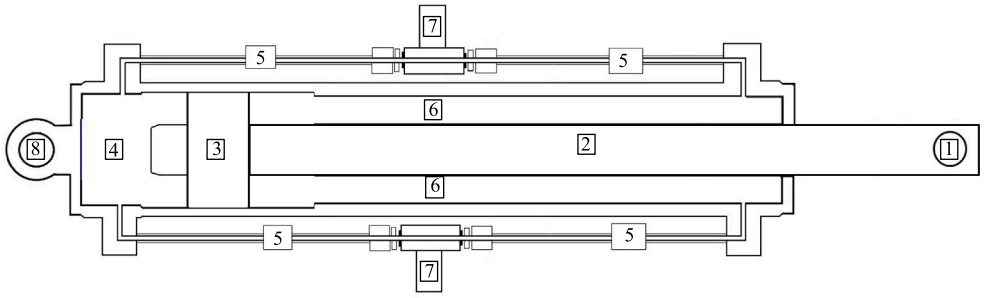

(b) Section view

Fig. 1. Details of ABFD device.

or failure which leads to misfunctioning of structure or machines.

Although provisions for bridge damages as a result of traffic loads have been defined in the bridge design procedure [14], more reliable techniques are still required. In 2020 a thorough evaluation has been conducted on European road bridges to verify the load model due to vehicle traffic [13]. Thus, the effects of traffic jams have been examined and the required safety margins or partial factors derived. The paper demonstrates the most frequently used load model is unable to represent the traffic action effects on the bridges.

Recently, Different types of restrainer systems and large-capacity damping devices developed to control the complex interaction between vehicle, environment, and the structure. In between, fluid dampers, when properly specified and designed, have served as a structure's primary defense to prevent catastrophic damage and costly repairs.

The resultant damping force from fluid dampers is proportional to the pressure difference across the piston head, expressed as a function of the velocity of the piston [10] and these dampers can operate over an ambient temperature ranging from − 40 °C to 70 °C [3]. In 2002, a developed case study was reported on the seismic response of a newly built 19/5 highway overcrossing in California that was equipped with fluid dampers. In this case study, the bridge was decomposed into its major sub-structural components, and the mechanical behavior of each sub-structural element was subsequently analyzed [12].

Additionally, the variable damping dampers were proven to be particularly appropriate for bridge structure vibration control since heavy traffic on highway bridges is known to be a source of impact loads that cause large vibrations. This long-term dynamic loading of the vehicles can reduce the expected service life of many highway bridges. Formerly, Patten [19] introduced the variable damping system into the actual engineering project to mitigate the vibration of the I-35 Bridge in America. The findings demonstrated that the semi-active variable damper was incredibly effective in increasing the total service life of the bridge by 35.8 years.

A pneumatic spring-oil damper with variable stiffness was used in a three-dimensional high-rise steel frame structure subjected to seismic loading by Huidong Zhang and Xujia Liu [32].

The dynamic analyses have been conducted for the 10- and 20-story structures equipped with new dampers and subjected to 5 typical ground motions. The results showed that the length, the inner diameter, and the initial pressure affect the structural dynamic demands and the parameters should be reasonably designed before engineering application.

A novel earthquake isolator system has been developed by using magnetorheological elastomer (MRE) material and the second-order sliding mode control has been implemented through semi-active control to mitigate the building vibration [29]. To achieve a high performance of MRE device-based, the nonlinear properties of the device has been developed and the field-dependent properties of the isolator identified due to varied currents and validated through experimental and numerical studies [30]. A shear-mode rotational MR damper with adaptive variable stiffness and damping has been implemented in the building structure to act as a real-time controller. The developed shear-mode rotational MR damper (SM-RMRD) as a semi-active control device proved to effectively control different earthquake vibrations and reduce the story acceleration and inter-story drift [31].

A new adaptive tuned viscous damper (ATVID) is introduced and damping properties of the ATVID-controlled were compared with the passive controlled and uncontrolled single-degree-of-freedom structures subjected to the variable-frequency harmonic ground excitation [20].

In another study, a series of mechanical experiments under various excitation frequencies and amplitudes were performed by Niwa and Kobori [18]. They obtained the curves of force–displacement hysteresis of the variable damping dampers used to control a steel office building in the city of Shizuoka. Eight dampers were mounted in the structure, and the results indicate that the installed dampers could substantially increase the structure's damping and were very efficient in reducing the steel structure's peak response.

Li et al. [11] designed and tested another kind of adjustable fluid damper in a 5-story steel structure. They compared the response of the structure with and without a semi-active damper on shaking table equipment under EL-Centro and Tianjin earthquake excitation, using the on/off algorithms. The findings showed that the supplementary damper

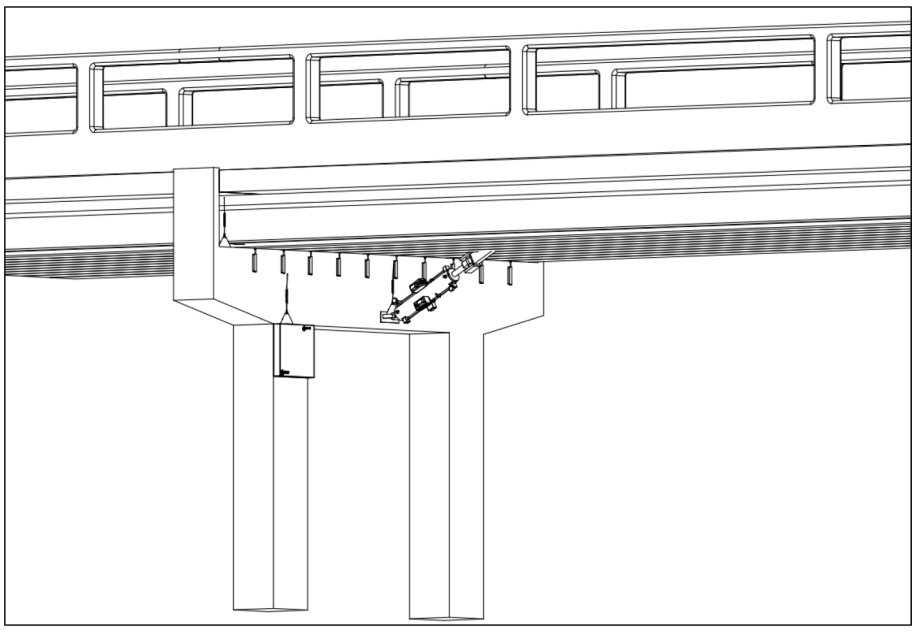

(a) Diagonal position

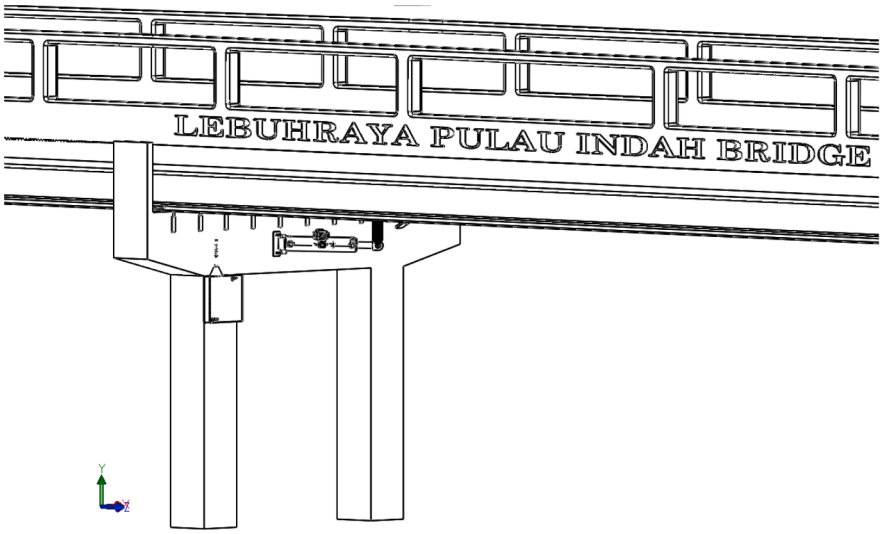

(b) Horizontal position

Fig. 2. The ABFD device installation position within the bridge structure.

mitigated the structural displacement and limited building movement for all modes of vibration.

Yang et al. [26] evaluated the influence of installing a variable damper to control dynamic responses of the structures, and the data indicate that the efficiency relies only on the ratio of the perturbation frequencies to the natural frequencies of structures.

A novel variable stiffness oil damper (ODVS) with a hydraulic cylinder and overflow valves was developed and placed in the transverse direction between the deck tower and the deck-pier connections [17]. The ODVS showed excellent stiffness to withstand wind and earthquake loads. The ODVS was developed to be a low-stiffness, high-damping damper.

The main objective of this study is to develop a new Adjustable Bypass Fluid Damper (ABFD) device consisting of a cylinder piston, and pair of bypass pipes with flow control valves. In this device, the flow rate of the fluid between two chambers of the cylinder is controlled by the opening position of the flow control valve. The valve position can be adjusted by the operator based on the required function of the device according to the response of the structure.

If the valves remain closed, the fluid flow from one chamber to another is restricted and high damping behavior is achieved. However, to achieve a low damping response, the fluid is allowed to flow freely through the bypass pipes in the fully open position of the valve. Finally, an intermediate damping level can be achieved by adjusting the flow control valves at a position between fully open and fully closed.

Thus, by adjustment of the valve position, the ABFD device functions as an adjustable viscous damper with different force and damping capacities or as act as a restrainer device to limit movement of the bridge deck under applied dynamic loads.

2. Development of the adjustable bypass fluid damper (ABFD)

In this research, a new Adjustable Bypass Fluid Damper (ABFD) has been developed. Assembled view and schematic diagram of the device

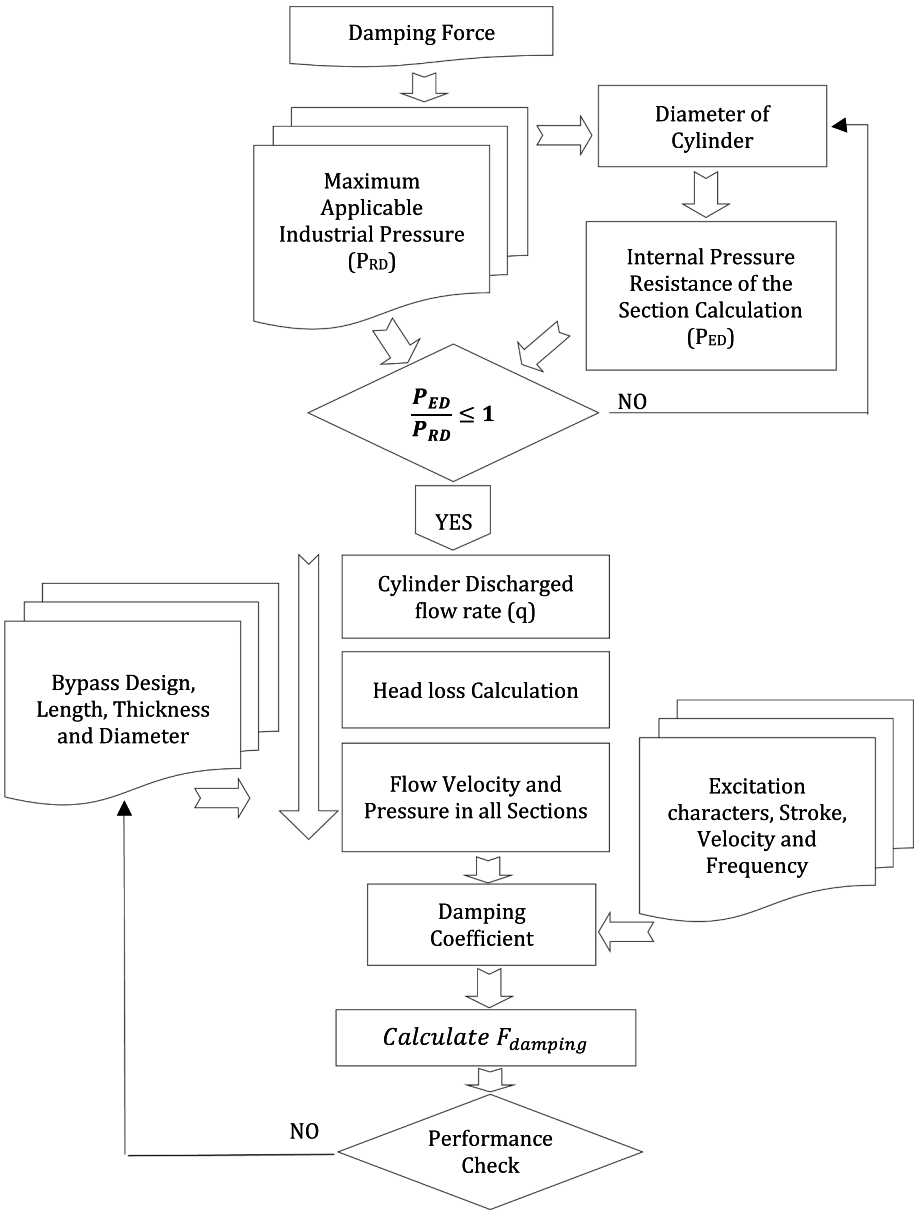

Fig. 3. ABFD primary design procedure.

are illustrated in Fig. 1 (a) and (b), respectively. The ABFD device mainly consists of a hydraulic cylinder (part 9 in Fig. 1 (a)), a piston, and two bypass pipes beside the cylinder (part 5). The piston comprises an end connector (part 1), piston shaft (part 2), and piston head (part 3). The Piston's head is considered to be rigid and without any holes or orifices and sealed inside the cylinder. Each bypass pipe, on the side of the cylinder, is equipped with a flow control valve. The opening of these two flow control valves can easily change to any position from the fully open position to the fully closed one. The opening value of the flow control valves changes the rate of the passing flow inside the pipes. Two pressure transducers (part 10) are embedded in the device to measure the pressure of the fluid inside the cylinder during the operation.

The ABFD device is connected to the structural members, i.e., bridge deck and piers, through the piston shaft connector (part 1) and hydraulic cylinder connector (part 8), respectively. This device can be installed within the bridge structure as a diagonal or horizontal braced member, between the bridge pier and deck as can be seen in Fig. 2 (a & b), and functions as a supplementary structural element to control the vibration response of the bridge structures due to vehicle traffic.

The dynamic load can be transferred from the structural member (bridge deck) to the piston shaft connector and push/pull the piston shaft (part 2) to the left/right side while the hydraulic cylinder connector (par 8) is fixed to the other structural members (bridge pier). So, the piston head (part 3) starts to move and the volume of the left/right chamber of the cylinder (part 4 / part 6) decreases. So, the fluid starts to travel through bypass pipes (part 5) to the right/left chamber of the cylinder (part 6 / part 4). The flow control valves (part 7) that are located in the middle of each pipeline are regulated and control the fluid flow rate passing through the pipes from one chamber to another. The movement of fluid from a larger area (cylinder chamber) to a smaller area (bypass line) and from a smaller area (bypass line) to a larger area (cylinder chamber), results in the energy dissipation base on the head loss energy phenomena.

In the ABFD device, when the valves are in their fully open states, fluid can flow freely through the bypass pipes so the device performs the lowest damping characteristics. In contrast, when the fluid is restricted, valves are in the fully closed position and the ABFD device generates the maximum resistant force.

Table 1
ABFD Geometrical Parameters.

Cylinder			Pipe		
Length (m)	Diameter (m)	Thickness (m)	Length (m)	Diameter (m)	Thickness (m)
0.976	0.175	0.0125	0.8	0.015	0.0218

Table 2
Mechanical properties of the fluid.

Density (15 °C)	0.88 kg/m^3
Relative Vapor Density (air = 1)	>1
Viscosity	65 mm^2/s@40 °C;8.6 mm^2/s@100 °C

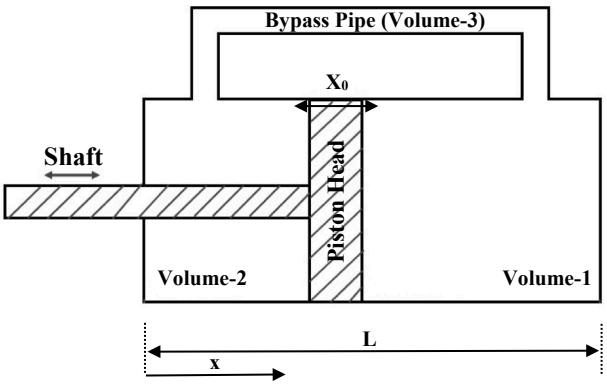

Fig. 4. The simplified diagram of the ABFD device.

3. Operational bound for the ABFD device

The design procedure of the ABDF device is demonstrated in the flowchart depicted in Fig. 3. To define the geometrical and mechanical properties of the hydraulic cylinder and hydraulic fluid, the availability of material, manufacturing, and test limitations have been considered.

According to the limitation of test equipment, the maximum excitation force has been considered to be equal to 300 kN with a maximum frequency of 1 Hz.

In this study, the temperature is considered as 30°c degrees, equivalent to environment temperature, for analytical prediction and also experimental testing. However, to maintain the considered temperature during the experimental test, enough rest time has been considered between each cycle to avoid any heating and rising temperature during conducting the test.

To design the hydraulic cylinder, the availability of material and manufacturing facilities have been considered. To choose the proper hollow steel tube, the first essential parameter is the maximum pressure that the hollow steel tube can resist according to the material properties and the thickness of the cylinder. The same maximum pressure has been checked for all other parts of the device during the manufacturing process, such as the valve, joints, and welding parts.

According to maximum force, and based on the available steel tubes, the cross-section area and the diameter of the cylinder have been defined, and at the same time, the length of the device has been calculated based on the required stroke of movement. The selected dimensions and mechanical properties of the device are listed in Tables 1 and 2.

The maximum internal pressure that applies to the cylinder during the operation (P_{ED}) is assumed to be less than the maximum allowable pressure (P_{RD}). This condition is also applicable when operation ceases abruptly and a surge occurs. So, the criteria from Eq. (1), are always assumed to be fulfilled.

$$\frac{P_{ED}}{P_{RD}} \leq 1 \tag{1}$$

To introduce the maximum and minimum damping characteristics of the device, the operational band, firstly, the analytical model of the device developed, and the fluid characteristics inside the cylinder and bypass pipes have been defined during the operation of the device.

3.1. Development of the analytical model

To develop the analytical model of the ABFD device, as an early assumption, the response of the damper is assumed to be equal to the displacement of the piston head. A simplified diagram of the ABFD device appears in Fig. 4. Originally, the pressure on the left/right chamber of the piston is equal. When the piston begins moving from its equilibrium point to the right, the pressure in volume-1 (in Fig. 4) rises due to compression, while pressure in volume-2 decreases due to rarefaction. The fluid then starts to flow from volume-1 to volume-2 through the bypass pipe, volume-3. As a result, the pressure in volume-1 decreases, and that increases the pressure in volume-2, and as long as the volume-1 pressure is greater than that in volume-2, the flow path stays the same. When the piston head moves in the reverse direction, the pressure in volume-2 is more than that in volume-1, and the flow in the bypass pipe will flow reversely. As an assumption, the friction between the piston and the cylinder is considered to be zero.

The flow rate in the bypass pipe due to the piston movement, considering the conservation of mass in volume-1, can be given as [9] Eq. (2):

$$\frac{dM_{32}}{dt} = A_{cl}\rho_1\frac{dX}{dt} - A_{cl}(L-X)\frac{d\rho_1}{dt} \tag{2}$$

where A_{cl} is cylinder cross-section area, ρ_1 is the fluid density in volume-1 and $\frac{dM_{32}}{dt}$ is the mass flow rate through the bypass pipe. L and X are highlighted in Fig. 4. The mass flow rate can also be written due to the volume-2 continuity equation, as Eq. (3):

$$\frac{dM_{32}}{dt} = A_{cl}\rho_2\frac{dX}{dt} + A_{cl}X\frac{d\rho_2}{dt} \tag{3}$$

where ρ_2 is fluid density in volume-2. Since the oil is considered to be incompressible, the density of the fluid in both chambers, ρ_1, and ρ_2, assumed to be identical, ρ, and constant during the operation, $\frac{d\rho_1}{dt} = \frac{d\rho_2}{dt} = 0$. So, the mass flow rate in bypass pipe can be written as follows:

$$\frac{dM_{32}}{dt} = A_{cl}\rho\frac{dX}{dt} \tag{4}$$

On the other hand, the fluid mass flow entering the volume-3, bypass pipe, can be demonstrated as Eq. (5):

$$\frac{dM_{32}}{dt} = v_{pp}\beta A_{pp}\rho \tag{5}$$

where v_{pp} is flow velocity inside the pipe and A_{pp} is the cross-section area of the pipe. Parameter β is shown the position of the valves in percentage, i.e., β equal to 75 % shows valves are 75 percent closed. The flow velocity inside the pipe can be obtained from Eqs. (4) and (5) as follows:

$$v_{pp} = \frac{A_{cl}}{\beta A_{pp}}\frac{dX}{dt} \tag{6}$$

The pressure inside the bypass pipe is computed from Bernoulli's Equation for volume-1 and volume-3 in Fig. 4.

$$\frac{V_1^2}{2g} + \frac{p_1}{\rho g} + z_1 = \frac{V_3^2}{2g} + \frac{p_3}{\rho g} + z_3 + h_L \tag{7}$$

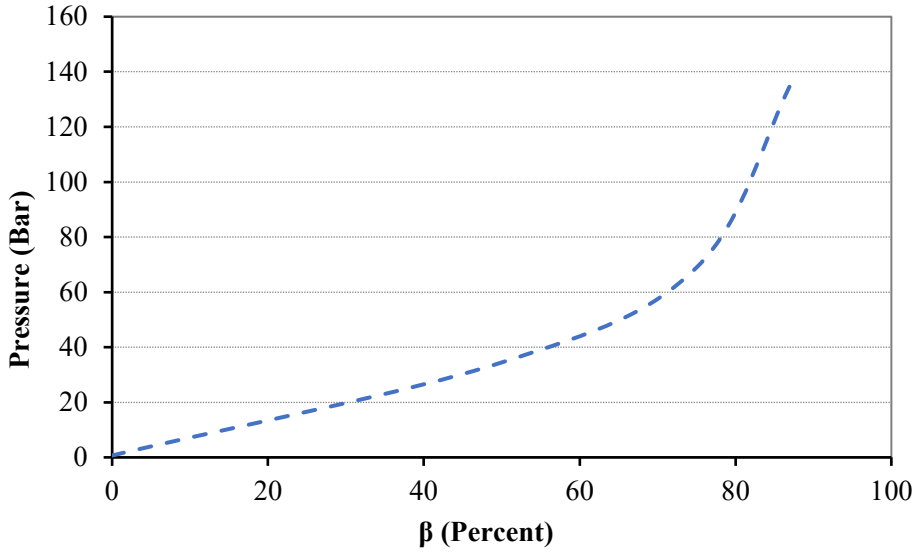

Fig. 5. Fluid pressure in the bypass pipes according to β, valve closing position.

where v_1, v_3, and p_1, p_3 are fluid velocity and pressure in volume-1 and volume-3, respectively. While evaluating the fluid flow, the effect of the boundary of the cylinder has not been considered. Parameter g is the gravity acceleration and when the damper is installed horizontally, $z_1 = z_3$. Total flow head loss, h_L, which is the essential parameter in providing damping of the device is divided into the major head loss and the minor head loss and can be demonstrated as:

$$h_{L=}h_{Lmajor} + h_{Lminor} \tag{8}$$

The minor and major head loss parameters consider the pressure drops due to viscous effects caused by an elbow and valve and are calculated through Eqs. (9) and (10).

$$h_{Lminor} = k_L \frac{{v_{pp}}^2}{2g} \tag{9}$$

$$h_{Lmajor} = f \frac{L_{pp}}{D_{pp}} \frac{{v_{pp}}^2}{2g} \tag{10}$$

where K_L is a minor head loss coefficient and is equal to 0.5 for the Sharp-Edged entrance of the pipe, [2].where f is Friction Factor, L_{pp} is pipe length, D_{pp} shows pipe internal diameter. By computing the pressure inside the bypass pipe the total pressure drop can be obtained. The friction factor value according to geometrical parameters is given by the Blasius equation (Avci and Karagoz, 2019). The damping coefficient of the damper device is demonstrated as Eq. (11):

$$C = \left[\frac{\rho A_{cl}^3}{2A_{pp}^2}\right]\left[K_1 + K_f\right]v_{pp} \tag{11}$$

where $K_f = \frac{fl_{pp}}{d_{pp}}$, and K_1 is the loss coefficient due to entry pressure loss and can be defined through Eq. (12) for volume-1 and volume-2:

$$\frac{p_1 - p_2}{\rho} = \frac{1}{2}\left[1 + \frac{fL_{pp}}{D_{pp}}\right]V_{pp}^2 + K_1\frac{V_{pp}^2}{2} \tag{12}$$

The calculated pressure using Eq. (12), for volume-2 and volume-3 according to the valve position is presented in Fig. 5.

As it can be seen from this graph, when the valves begin to close from the fully open condition, the upstream pressure inside the bypass pipe starts to rise. Whereas the pressure the downstream, after valves, drops. When β increases more than 75 % and the valves open 25 percent or less, the slope of the curve increases dramatically. Therefore, it can be concluded that the ABFD device performance is more sensitive to the

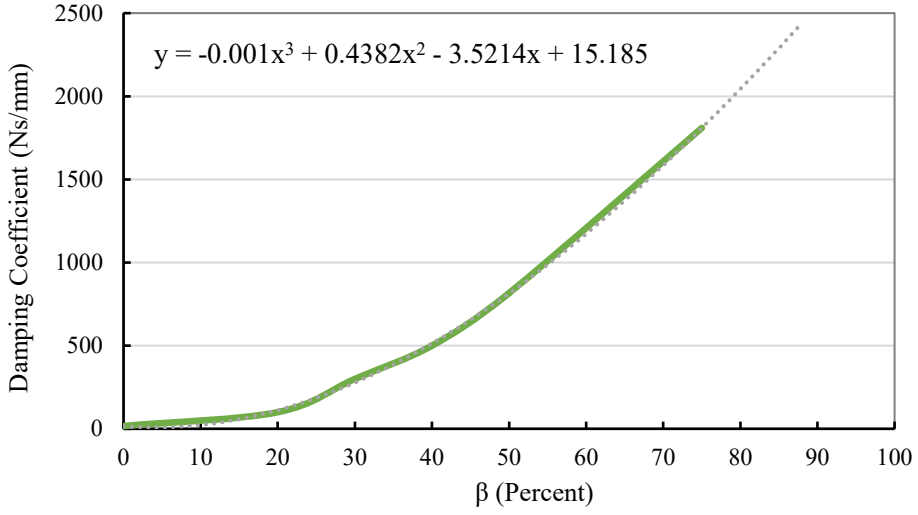

Fig. 6. Numerically predicted damping coefficient of the ABFD device according to the valve position.

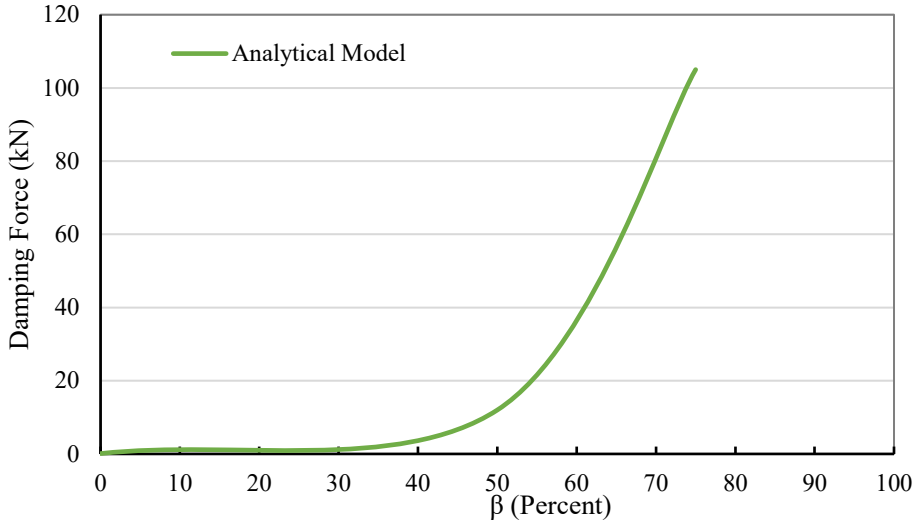

Fig. 7. Numerically predicted damping force of the ABFD device according to valve state.

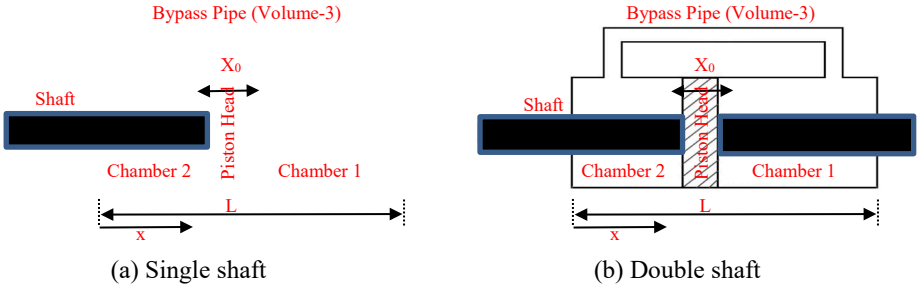

Fig. 8. The simplified diagram of the double-side shaft piston.

valve position when β is bigger than 75 %. Accordingly, the damping coefficient parameter changes with β are calculated from Eq. (11) and are depicted in Fig. 6.

The variation of the damping coefficient can be extracted from the graph as Eq. (13).

$$C = -0.001\beta^3 + 0.4382\beta^2 - 3.5214\beta + 15.185 \quad (13)$$

Thus, the numerical computations predict the damping coefficient of the ABFD damper is raised with the increase of the β, i.e., closing the valves. When the valve is almost closed, β > 75 % damper function changes from the damper to a restrainer, so the damping coefficient drops to zero for the fully closed valve. Finally, the damping force of the damper can be calculated from the pressure differences between chambers 1 and 2 as Eq. (14). This Equation can be extended to calculate

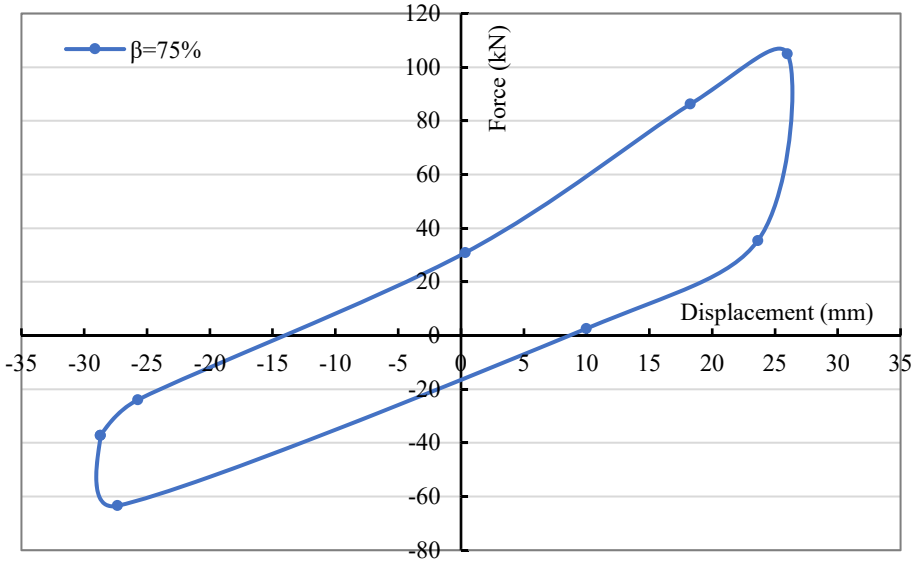

Fig. 9. Force-displacement prediction for β = 75 %.

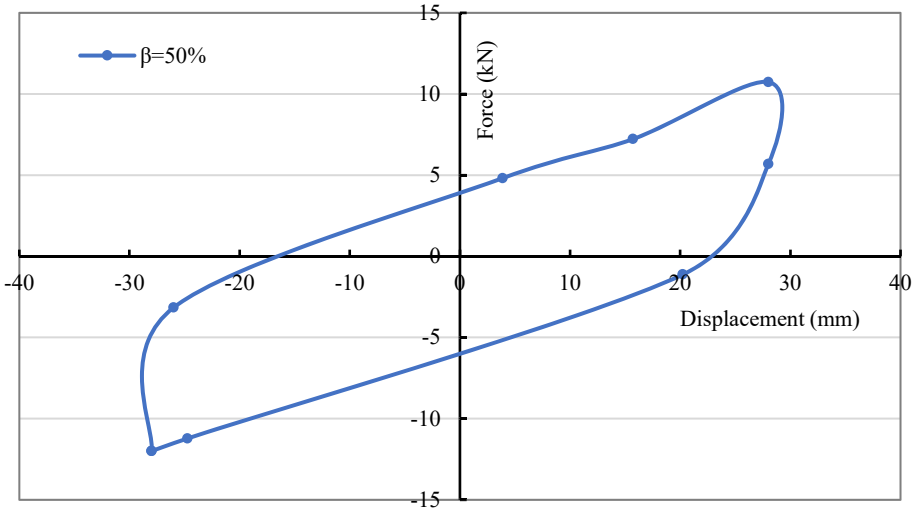

Fig. 10. Force-displacement prediction for β = 50 %.

Table 3
ABFD device working range.

Maximum Allowable Internal Pressure (P_{ED})	4000 Psi (27.58 MPa)
Minimum / Maximum Excitation Velocity (mm/s)	0.03/0.07
Minimum / Maximum Damping Coefficient (N.s/mm)	16.5/1809
Minimum / Maximum Damping Force (kN)	0/105

the resistant force of the device for Beta higher than 75 % which affects the pressure differences between two chambers.

$$F_{Damping} = (A_{cl})^2 \bullet (p_2 - p_1) + A_{Shaft} \bullet p_2 \tag{14}$$

where A_{Shaft} is the occupied cross-section area by the shaft. So, the adjustable damping force of the ABFD device is numerically predicted and depicted in Fig. 7. This graph estimates the damping performance of the device is increasing with closing the valve.

As can be seen in Fig. 8 since the shaft core occupied a considerable volume in chamber 2 of the hydraulic cylinder, the section areas of chamber 2 are much smaller than the section area in chamber 1, therefore, this difference is led to have different volume of oil to flow during pulling and pushing which caused the asymmetric force–displacement results. However, to avoid this issue, a double side shaft piston can be used to have the same flow amount on both sides which resulted in symmetric force–displacement action in pulling and pushing.

The equation corresponding to the asymmetric condition of the device has been implemented and the new force–displacement graphs have been plotted in Figs. 9 & 10 for β equals 50 % and 75 %.

By the use of calculated data from the analytical model, the testing equipment and hydraulic jack limitations, the upper and lower

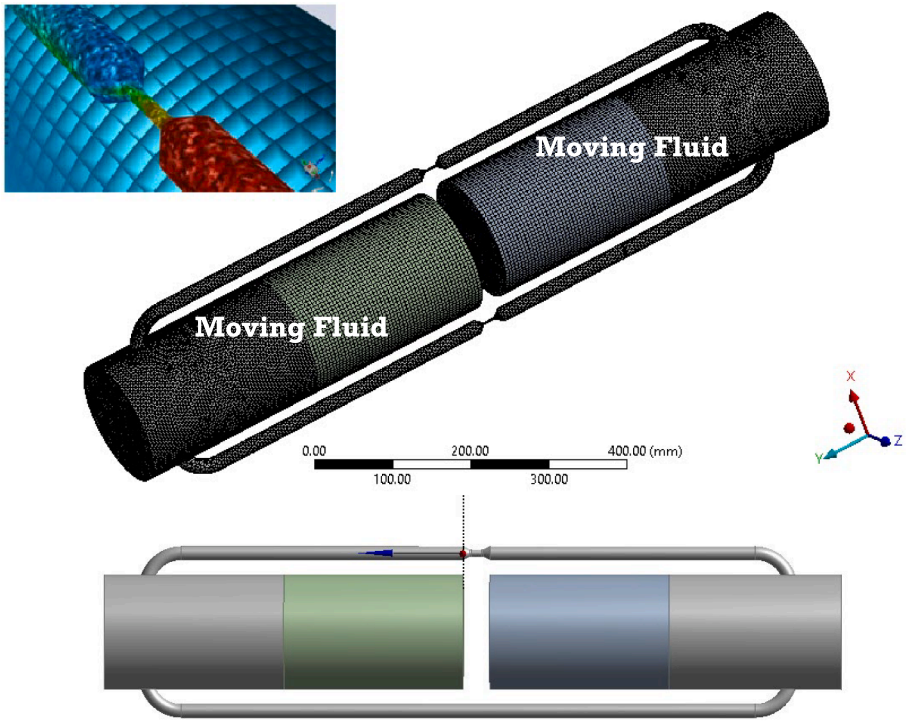

Fig. 11. The applied mesh and boundary conditions in the CFD model.

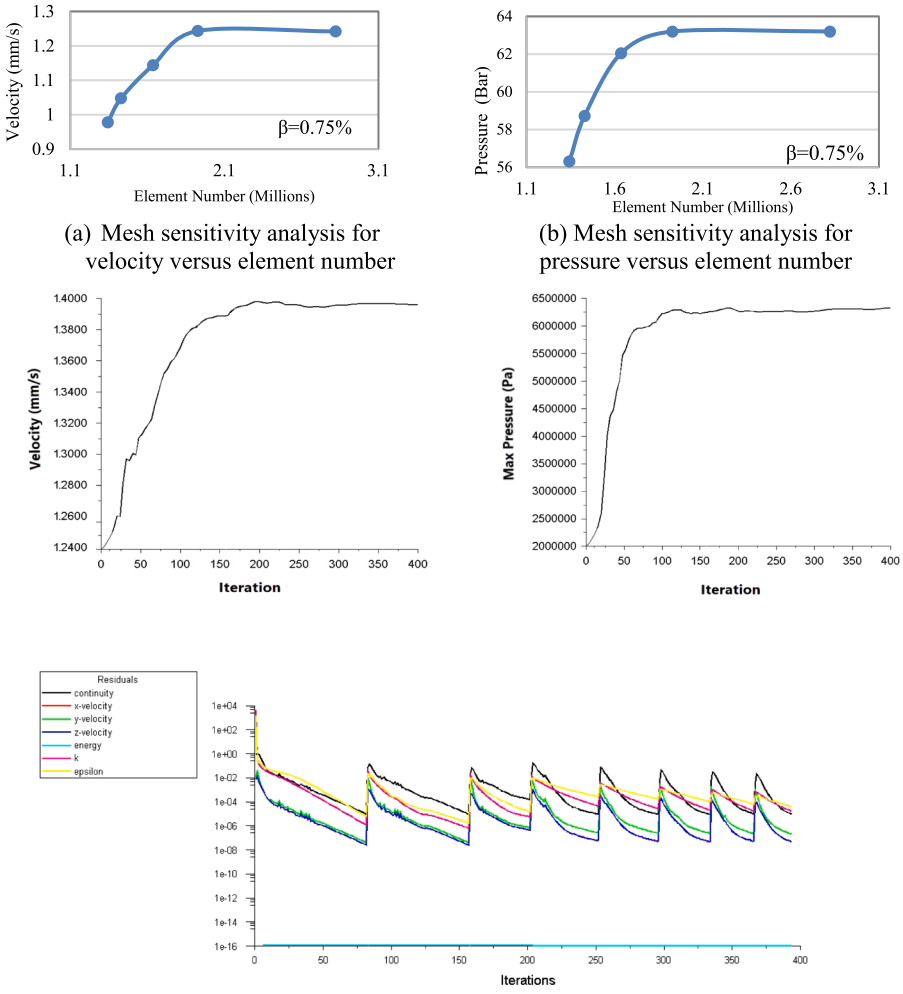

(a) Mesh sensitivity analysis for velocity versus element number

(b) Mesh sensitivity analysis for pressure versus element number

(e) Convergency analysis for monitoring of Residuals

Fig. 12. Mesh sensitivity and convergency analysis for finite element model.

operational limit, the geometry, boundary condition and the material specifications of the ABFD device can be introduced. These data are summarized in Table3.

3.2. *Development of the finite volume model*

During the operation, the fluid flows inside the hydraulic cylinder and bypass pipes according to the movement of the piston head. The piston head divides the hydraulic cylinder into two separate chambers. The length of these chambers changes due to the piston head movement. Therefore, the size of the fluid domain varies as the piston head moves. So, the flow equations are functions of time and solutions are inherently unsteady. To develop the finite volume model of the fluid flow inside the damper, the dynamic mesh technique is utilized and the Layering method was applied to shift elements boundaries and change the mesh configuration with time appropriately.

In this method, cells were inserted or removed, and internal node positions were determined automatically based on boundary motion, cell size, and predefined mesh structure. An unsteady solver was set up for the dynamic mesh configuration. Since the head of the piston moves during the operation and pushes the oil, a moving domain with moving boundaries has been implemented to simulate the device. [6 16].

At each time step, the new position of the piston head is computed. Then the dynamic mesh model updates the grid and the unsteady flow field is integrated to calculate the flow velocity and pressure. The piston motion of 30 mm with a velocity of 25, 30, and 45 mm/s was considered and applied in two different load steps in the positive and negative Y direction (Fig. 11). To determine piston head displacements, two moving walls have been considered and defined in dynamic mesh zones using UDF codes. The inner surface of the cylinder is fixed to the wall and the area inside the damper is covered by the fluid for flow analysis. The moving walls, moving fluid domain, applied mesh, and boundary conditions are illustrated in Fig. 11.

Ansys workbench 2019 R1 has been utilized for the flow simulation presented in this study. Changing of β parameter is applied in the pre-processing step by changing the geometry at the valve position in the bypass pipe. For instance, Beta equal to 75 % is modeled by decreasing the area to 75 percent of the bypass pipe area. The combination of 1,928,080 Hexahedron and Tetrahedron elements was used to simulate the damper device.

The mesh independence study also has been conducted for all simulations. The results for mesh sensitivity analysis (Fig. 12) revealed that increasing the number of elements from 1,343,836 to 1,637,910 by using fine mesh, affected the results for velocity and pressure inside the fluid domain. However, for higher mesh resolution, when the number of elements is more than 1,928,080, the analysis outcomes are stable and independent of the number of elements.

Also, as shown in Fig. 12, the result for monitoring of convergency indicated that the convergency of the analysis has been achieved through 400 iterations. Also, to monitor the convergency procedure, two

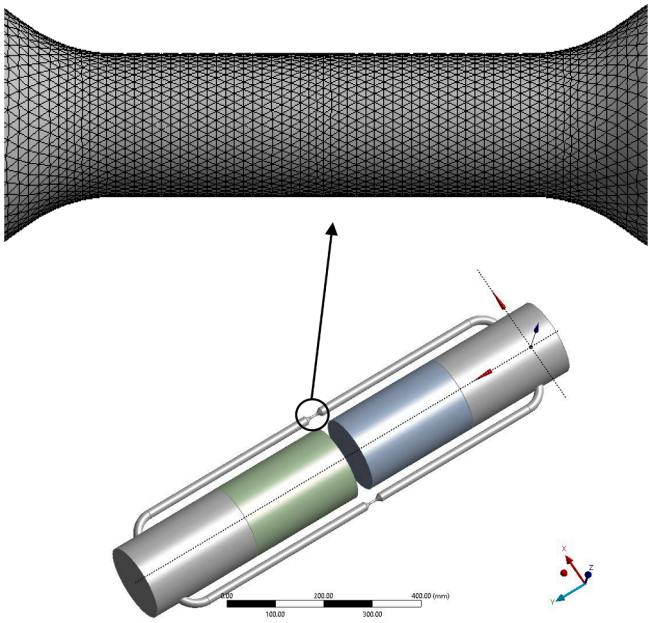

Fig. 13. Simulating valve opening state at β = 50 %.

main parameters inside the cylinder as maximum velocity and maximum pressure have been defined and monitored as shown in the plots. As it can be seen in the graphs, all considered parameters are getting stable in 400 iterations to converge the analysis procedure.

The integral form of the conservation equation for a general scalar, ϕ, on an arbitrary control volume V, whose boundary is moving, can be written as Eq. (15).

$$\frac{d}{dt}\int_V \rho \varnothing dV + \int_{\partial V} \rho \varnothing \left(\overrightarrow{u} - \overrightarrow{u_g}\right) d\overrightarrow{A} = \int_{\partial V} \Gamma \nabla \varnothing d\overrightarrow{A} + \int_V S_\varnothing dV \tag{15}$$

where ρ is the fluid density, $\overrightarrow{v}$ is the flow velocity vector, $\overrightarrow{u_g}$ is the mesh velocity of the moving mesh, Γ is the diffusion coefficient, and S_ϕ is the source term of ϕ. While ∂V is used to determine the boundary of the control volume V. The time derivative term in Eq. (16) can be written, using a first-order backward difference formula, as follows [4].

$$\frac{d}{dt}\int_V \rho \varnothing dV = \frac{(\rho \varnothing V)^{n+1} - (\rho \varnothing V)^n}{\Delta t} \tag{16}$$

where n and n + 1 denote the respective quantity at the current and next time levels. The (n + 1) the time level volume V n + 1 is computed from:

$$V^{n+1} = V^n + \frac{dV}{dt}\Delta t \tag{17}$$

where dV/dt is the volume-time derivative of the control volume. The volume-time derivative of the control volume is calculated as Eq. (18) to fulfill the mesh conservation law.

$$\frac{dV}{dt} = \int_{\partial V} \overrightarrow{u_g} \bullet d\overrightarrow{A} = \sum_j^{n_f} \overrightarrow{u_{gj}} \bullet \overrightarrow{A_j} \tag{18}$$

where n_f is the number of faces on the control volume, and A_j is the j face area vector. The dot product $u_{gj}.A_j$ on each control volume face is calculated from:

$$\overrightarrow{u_{gj}} \bullet \overrightarrow{A_j} = \frac{\rho V_j}{\Delta t} \tag{19}$$

where ρV_j is the volume swept out by the control volume face j over the time step Δt.

In the case of the sliding mesh, the motion of moving zones is tracked relative to the stationary frame. Thus, to simplify the flux transfers across the interfaces, no moving frames are attached to the computational domain. In the sliding mesh formulation, the control volume stays constant, so from Eq. (17), dV/dt and $V_{n+1} = V_n$. Eq. (18) can now be expressed as follows:

$$\frac{d}{dt}\int_V \rho \varnothing dV = \frac{\left[(\rho \varnothing)^{n+1} - (\rho \varnothing)^n\right] V}{\Delta t} \tag{20}$$

The well-known Navier–Stokes's equations are used for modeling the incompressible turbulent flow inside the ABFD device. The Navier–-Stokes's equation Continuity and Momentum equations are determined as follows, respectively.

$$\nabla \bullet U = 0 \tag{21}$$

$$\frac{\partial U}{\partial t} + (U \bullet \nabla) \bullet U + \nabla P = \frac{\mu}{\rho}\left(\nabla^2 U\right) \tag{22}$$

In addition, different β values, valve opening states, are modeled by changing the cross-section area of the bypass pipe beneath the valve as shown in Fig. 13.

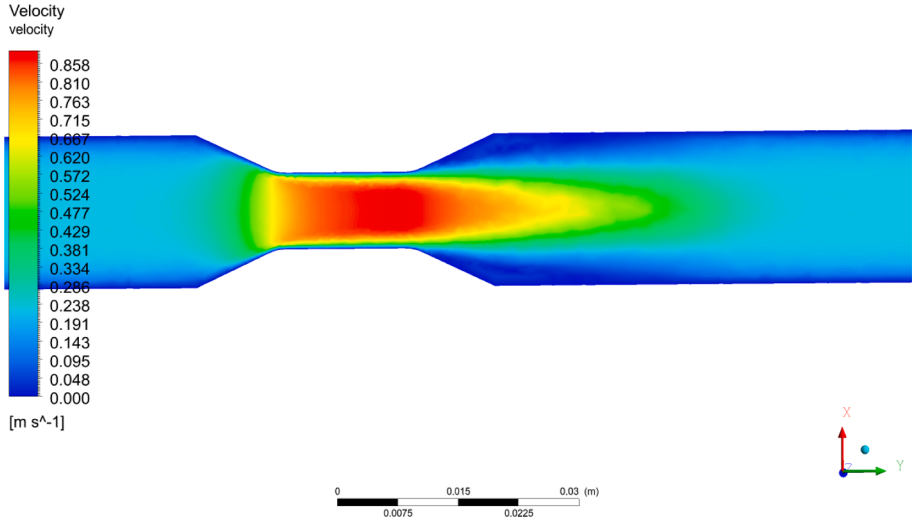

Fig. 14. Velocity contour at valve position in bypass pipes of the ABFD device.

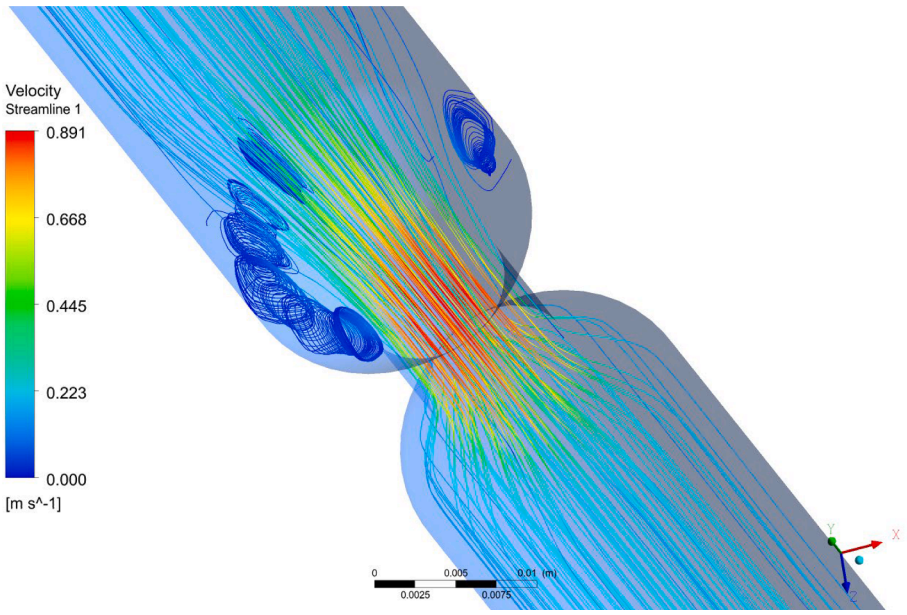

Fig. 15. Velocity streamline contour at valve position in bypass pipes of the ABFD device.

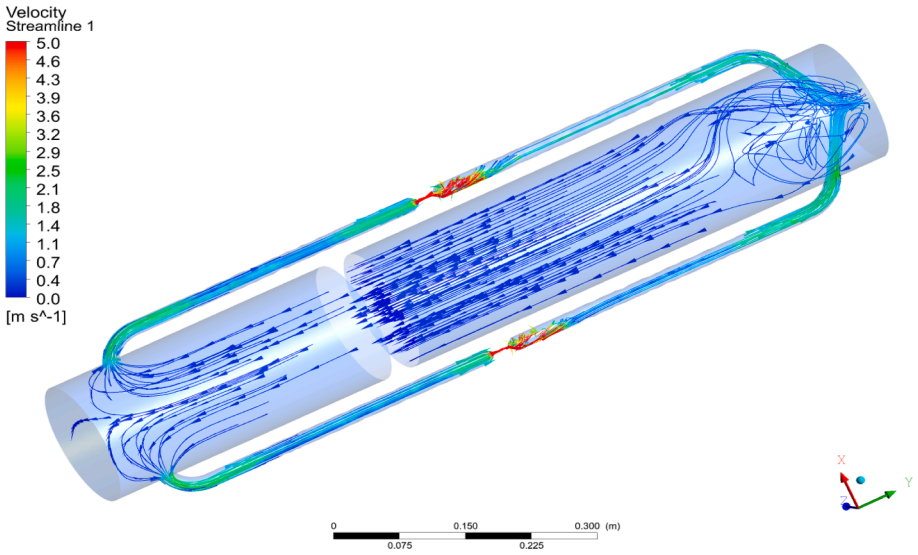

Fig. 16. Velocity streamline contour in the ABFD device during operation.

3.3. Finite volume analysis results for ABFD

Finite volume resultant data include velocity and pressure contours and graphs are presented in this section. Velocity contour at valve position in bypass pipes is illustrated in Fig. 14.

This contour is revealing the rising velocity of the fluid flow when the pipe cross-section area decreases as a result of the closing valve. In this case, the valve area is functioning like a nozzle-diffuser system and increases the flow velocity while reducing the flow pressure. The flow streamlines in Fig. 15 also show not only the fluid speed up downstream but also there is flow separation phenomena at the valve area. The generated wakes due to the boundary layer separation can be amended by the proper design of the valve-pipe joint area. Otherwise, the produced eddies and vortices will result in an adverse pressure gradient and lower efficiency.

Depicted velocity streamlines in Fig. 16 in the hydraulic cylinder show the flow behavior during piston movement. As can be seen in this contour, the piston head is moving from left to right; so, while the volume of the left chamber is decreasing, the fluid flows from the left chamber towards the right chamber. The pattern of the streamlines shows the wakes and separation of the boundary layer in the right chamber, where the volume is increasing and the pressure drops. The pressure contour is demonstrated in Fig. 17 and reveals the pressure variations of the fluid flow when the valve is closed. In this figure, the pressure from the left side, upstream, to the right side, downstream decreases.

The patterns of the velocity and pressure variations are depicted in Fig. 18. The graph shows by closing the valves, at flow downstream, the velocity increases, and the pressure drops. During the operation, it is necessary to keep the pressure of the fluid above the fluid saturation pressure. The arrangement of the system is required to be set so that piston can complete its action without causing a vacuum in different chambers of the cylinder. The valve position and initial pressure inside the cylinder are the main parameters that should be considered in the procedure design. The velocity and pressure are varying smoothly while the valve is open more than 25 % percent but for the β bigger than 75 %,

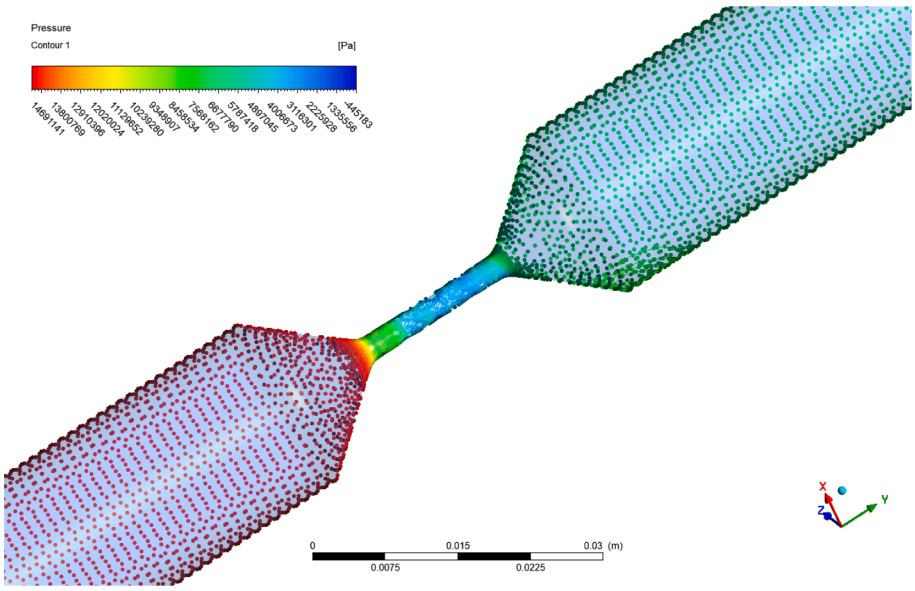

Fig. 17. Fluid flow pressure at valve position in bypass pipes of the ABFD.

the flow characteristics vary significantly with any changes in valve position. Therefore, this pattern proves that a very accurate control procedure is required to regulate damper parameters in this range.

4. Fabrication of the prototype and experimental data

The piston head and piston shaft are illustrated in Fig. 19 (a) and (b), respectively. As it can be seen in this figure, the piston head is made from rigid steel plates with no orifice holes. The piston head is sealed thoroughly inside the hydraulic cylinder by the use of seal wires, Fig. 20 (a). The thread at the piston head-shaft joint has been designed so that it can resist 300 kN applied force, Fig. 20 (b).

Besides, parallel threads are provided with O-ring seals to make proper sealing against leakage to the outside on different parts of a hydraulic cylinder. The material used in sealing is specified with good sealing properties and proper resistance against the hydraulic fluid. All the fabrication procedure has been made based on the design geometrical parameters in Table 1. The bypass pipe thickness is shown in Fig. 21.

The hydraulic cylinder and the fabricated ABFD device are shown in Fig. 22 (a) and (b), respectively. The hydraulic circuit of the ABFD device was designed based on the variable fluid viscous damper studied by Symans and Constantinou [21] and it is shown in Fig. 23.

This circuit consists of two manual flow control valves which are installed in the middle of the bypass pipes. So, the amount of fluid passing through the external path is determined by the opening state of the flow control valves. The bypass pipes have been built through drilling cylinder and connecting routes on each side of the cylindrical casing. The flow control valves can persist to a maximum pressure of 345 bar (5000 Psi) and adjust the device's function from a damper when the valve is in the fully open position to a restrainer when the valve is fully closed.

To evaluate the performance of the prototype, several experimental tests including an incremental cyclic test and cyclic load frequency test have been conducted. For this purpose, an experimental test setup was fabricated and installed on the strong floor of the structural laboratory. The test setup is illustrated in Fig. 24. It can be seen that the setup is constructed from four main parts. Parts 1 and 2 show the back support and uplift restrainer for the dynamic actuator respectively, which hold the actuator in a fixed horizontal and vertical position. Parts 3 and 4 have the same function of holding the prototypes. However, part 4 contains an additional connection hinge to which the prototype is attached to it.

For the experiments, an electro-hydraulic actuator was used to implement a saw-tooth displacement pattern. The performance measurements of dampers were conducted based on the relationship of force–velocity-displacement and the comparison of the maximum velocity damping force with the assumed design value (JSSI [8]. The actuator is connected to the PLC control panel and data acquisition system through displacement LVDT sensors embedded in the test set-up. The schematic diagram of the test setup is shown in Fig. 25.

Also, to evaluate dampers, three or more cycles of loading were applied at a predefined condition 78uuu [22]. The fabricated ABFD prototype and the experimental test setup are illustrated in Fig. 26. The cyclic incremental displacements, according to Table 4 have been applied to the end joint plate of the piston of the ABFD device by the mean of the dynamic hydraulic actuator with 300kN load capacity.

4.1. Incremental cyclic test results

There were a series of experimental tests running over frequencies of 0.5, 0.75, and 1 Hz, and peak velocities of 30, 50, and 70 mm/s to evaluate the performance of the ABFD damper (Table 4). The frequency and the velocity of the applied force have been chosen according to the testing facilities operating range and capacity. The facilities in the structural laboratory of the University Putra Malaysia are designed to operate in a range of 0.5 Hz to 1 Hz since most structures are performing within this frequency range, therefore usually structural damper devices are tested in this range of frequency (JSSI, 2003).

The resultant experimental force–displacement hysteresis loops when the ABFD device is subjected to the 30 mm dynamic stroke displacement, push and pull, for different β values, 0, 50 %, 75 %, 87.5 %, and 100 % are depicted in Fig. 27 to Fig. 31, respectively. These results revealed that the change of the valve state regulates the performance of the ABFD from a passive fluid damper to a restrainer behavior. Fig. 27 demonstrated the ABFD device behavior when the valves are fully open. In this case, the device functions like a passive viscous damper and the damping force result from the friction. The maximum damping force in this valve state is about 1 kN which performs the minimum damping ratio and stiffness.

When the valves are half-closed, the maximum damping force rises to 17 kN, these data are demonstrated in Fig. 28. The value of maximum damping force increases again up to 120 kN with closing the valve to the state of $\beta = 75$ % in Fig. 29.

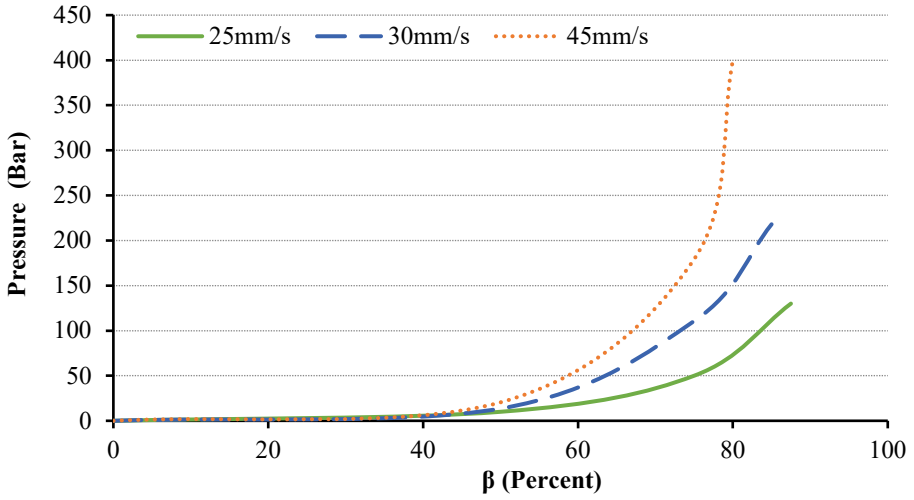

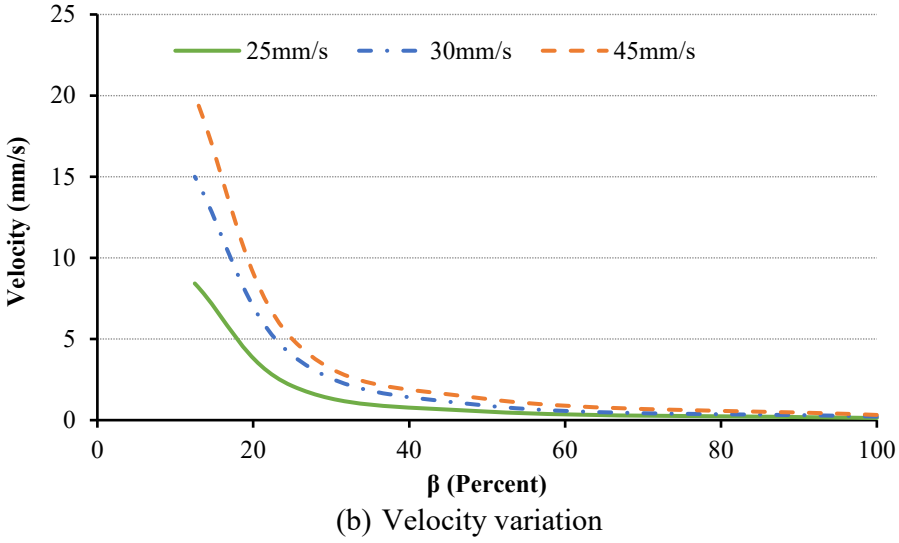

Fig. 18. Velocity and pressure variations in the pipe according to the valve position.

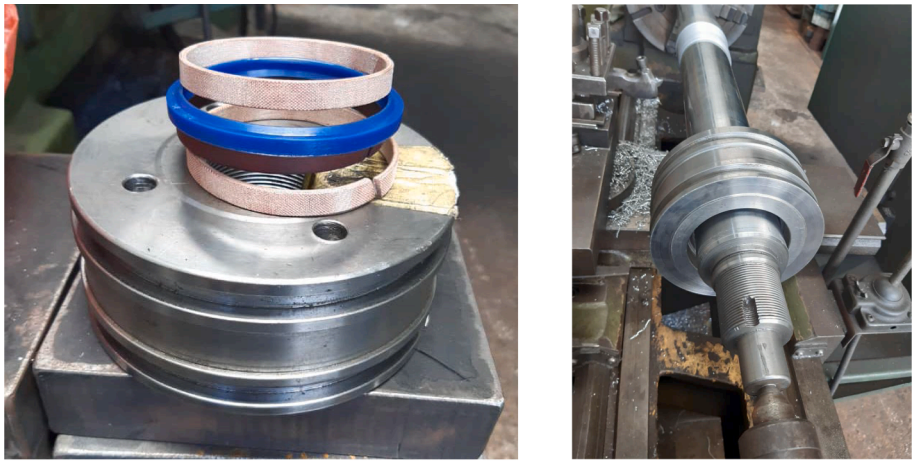

Fig. 19. Fabrication of the ABFD device.

Fig. 20. Fabrication of the ABFD device.

Fig. 21. Fabrication of the bypass pipes.

During experimental tests, it is noticed that small movements and shakings in the joints, hinges and connections were affected the stability of the results. Also, the tests have been conducted in low speed to control the temperature rise inside the cylinder but when the maximum displacements apply to the cylinder the temperature increases and cause some instability in the response loop.

When more than 25 % of the valves are closed, the device starts to function like a restrainer instead of a damper. In Fig. 30, it can be seen that the area inside the hysteresis loop decreases in comparison with the graph at $\beta = 75$ %. Then the device begins to resist the applied load and the oil pressure starts to increase dramatically. Therefore, the maximum applied load when β is greater than 75 % is not only limited by the device resistance force but also through the safety pressure control of the hydraulic circuit. So, the maximum load in Fig. 30 and Fig. 31 is limited to 100 kN and 80 kN, respectively. With the same pattern, the damping characteristics of the device significantly reduced for $\beta = 100$ %, when the valves are closed in Fig. 31.

Experimental tests revealed that when the applied displacement changes from 30 mm to 50 mm and 70 mm, the performance of the device follows the same pattern but the maximum damping load increases.

The resultant data for 50- and 70-mm displacement is depicted in Fig. 32 and shows that the maximum damping force increased up to 50 and 120 kN, respectively. Which is about 17 kN when 30 mm displacement is applied to the device (Fig. 28).

The resultant stiffness of the ABFD device from the experimental tests is depicted in Fig. 33. Results show that the stiffness values raise with closing the valve. This device can generate a damping coefficient in a continuous range between 16.5 and 2203 Ns/mm. Resultant experimental data including stiffness, damping coefficient, and damping exponent are summarized in Table 5.

To compute the effective stiffness and damping of the device for various β values, using the hysteresis response graph, the effective stiffness (k_{eq}) is determined through the slope of the straight line from the point of (maximum load, maximum displacement) to the point of (minimum load, minimum displacement). [24]

$$k_{eq} = \frac{f_m}{\Delta_m} \tag{23}$$

Whereas, effective damping is calculated by equating the energy absorption by the hysteretic steady-state cyclic response at a given displacement level, as expressed by [15]:

$$C = \frac{A_h}{2\pi f_m \Delta_m} \tag{24}$$

where Ah is the area of a complete cycle of force–displacement response and Fm and Δm are the maximum force and the displacement that occurred in the complete cycle respectively. The parameters to calculate effective damping is demonstrated in Fig. 34.

4.2. Cyclic load frequency test results

The experimental test has been repeated for 0.5,0.75, and 1 Hz different excitation frequencies, and the performance of the device was measured for different loading conditions. Fig. 35 shows ABFD device hysteresis loops under various excitation frequencies. The results of the load–frequency test have been summarized in Table 6. As it can be seen in the tabular data, the resultant damping force is increased when the frequency of imposed load raises. Thus, when the applied frequency is increased from 0.5 HZ to 0.75, and 1 HZ, the damping coefficient also increases about 1.89 and 3.37 times from 816 to 1540 and 2750 N.s/mm, respectively.

4.3. Validation of numerical result with experimental test

To validate the numerical results with experimental outcomes, firstly the pressure data of the fluid inside the hydraulic cylinder from all three methods, analytical calculations, finite volume simulation, and

Fig. 22. Fabrication of the ABFD device.

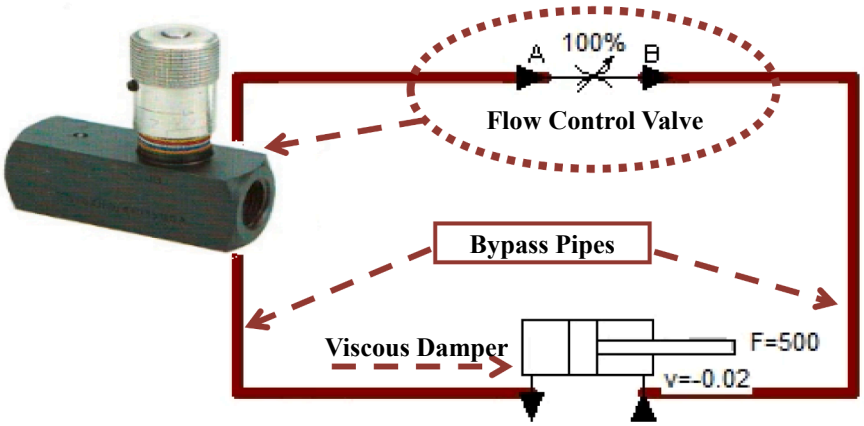

Fig. 23. The hydraulic circuit of the ABFD device.

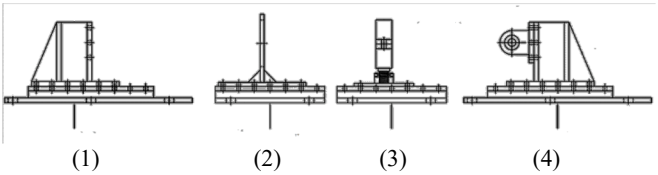

No.	Component
1	Actuator back support
2	Actuator uplift restrainer
3	Damper uplift restrainer
4	Damper back support

Fig. 24. Experimental test set-up.

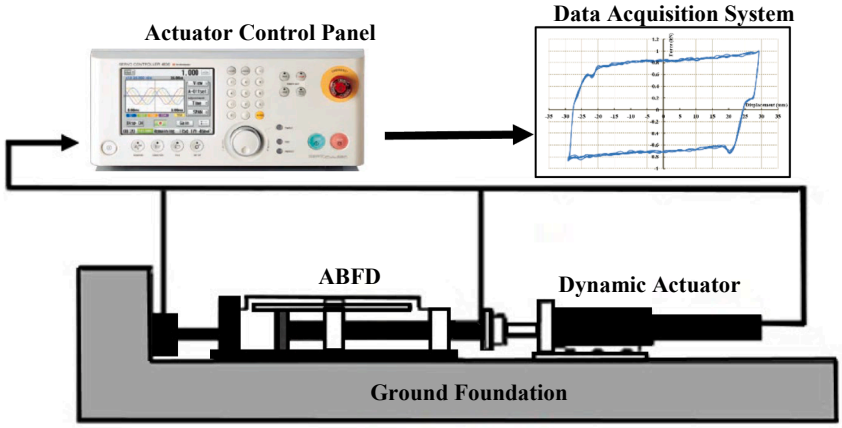

Fig. 25. Schematic diagram of ABFD experimental test set-up.

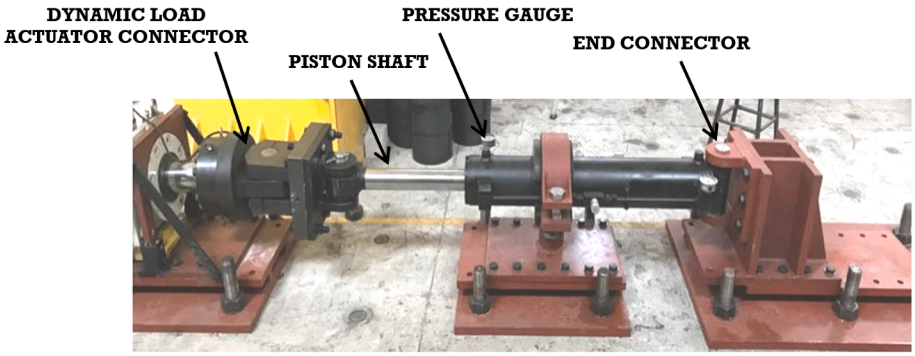

Fig. 26. Experimental test setup and the ABFD device installation.

Table 4
Excitation loads applied during experimental tests.

Maximum Load (kN)	300
Frequency (Hz)	0.5/0.75/1
Velocity (mm/s)	25/33/50
Displacement (mm)	±30/ ±50/ ±70

experimental tests, have been compared. This comparison is demonstrated in Fig. 36. The results extracted from all these three approaches with a very close agreement show the pressure inside the cylinder varies gradually when β is smaller than 75 % and then the slope of the pressure-β is increasing dramatically. So, these data were used to compute the overall damping characteristics of the damper, as is seen in Fig. 37 and Fig. 38. The computed data include the damping coefficient and damping force of the device. In the finite volume analysis, the perfect

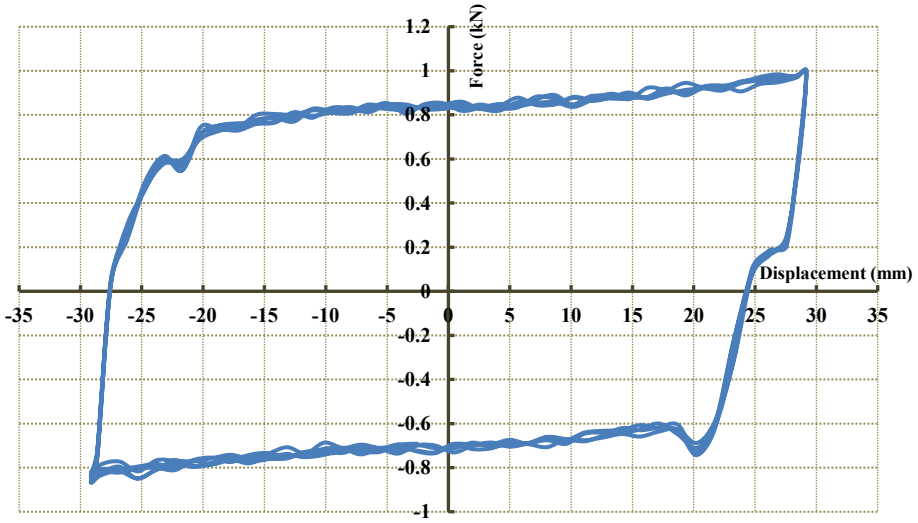

Fig. 27. ABFD hysteresis loop at fully open valves (β = 0).

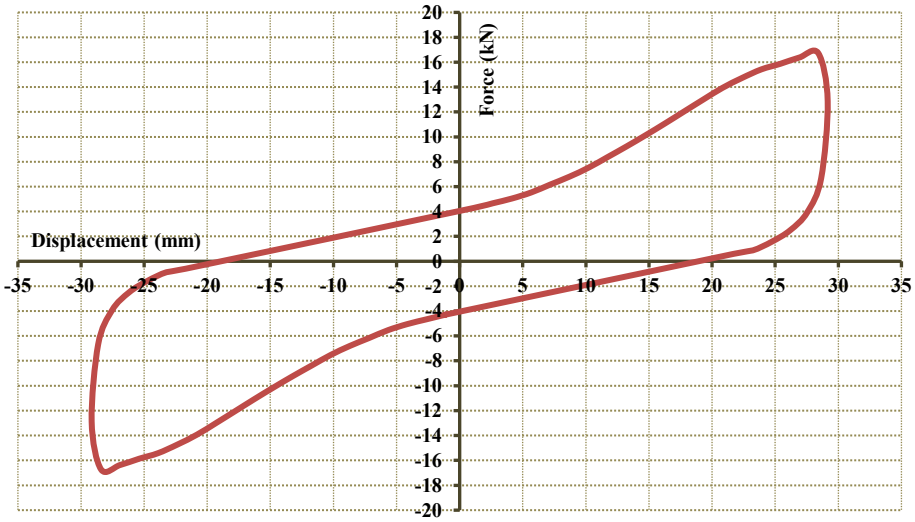

Fig. 28. ABFD hysteresis loop when valves are 50 % closed (β = 50 %).

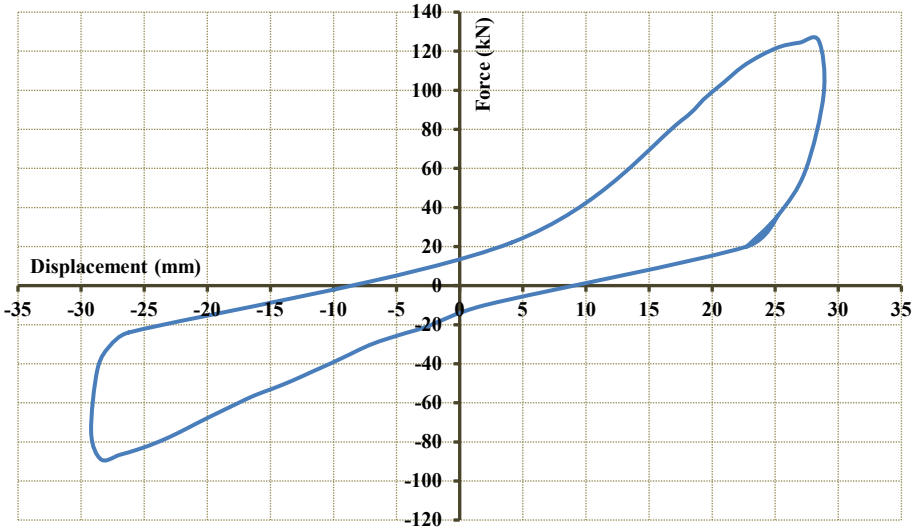

Fig. 29. ABFD hysteresis loop when valves are 75 % closed (β = 75 %).

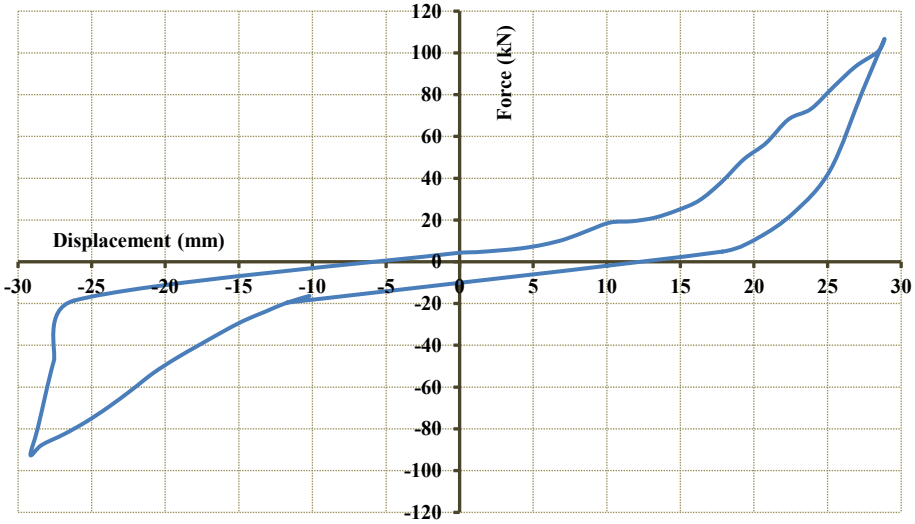

Fig. 30. ABFD hysteresis loop when valves are 87.5 % closed (β = 87.5 %).

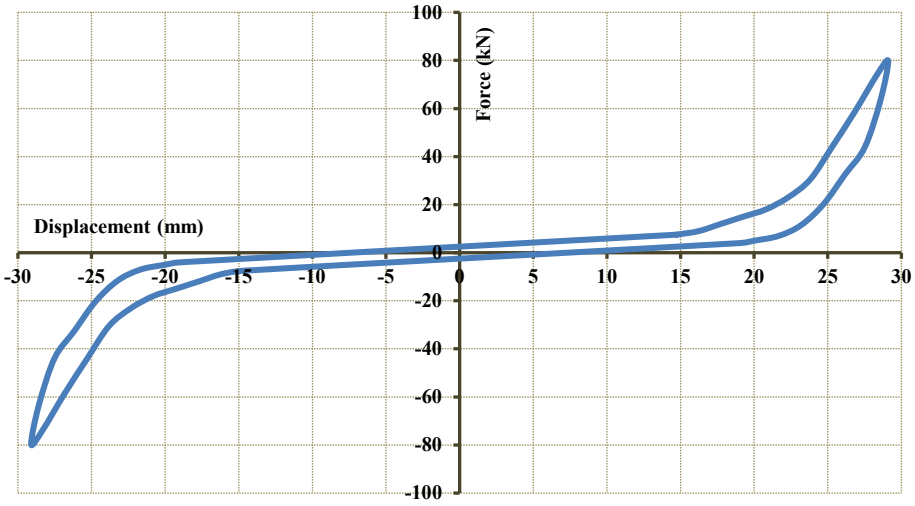

Fig. 31. ABFD hysteresis loop at fully closed valves (β = 100 %).

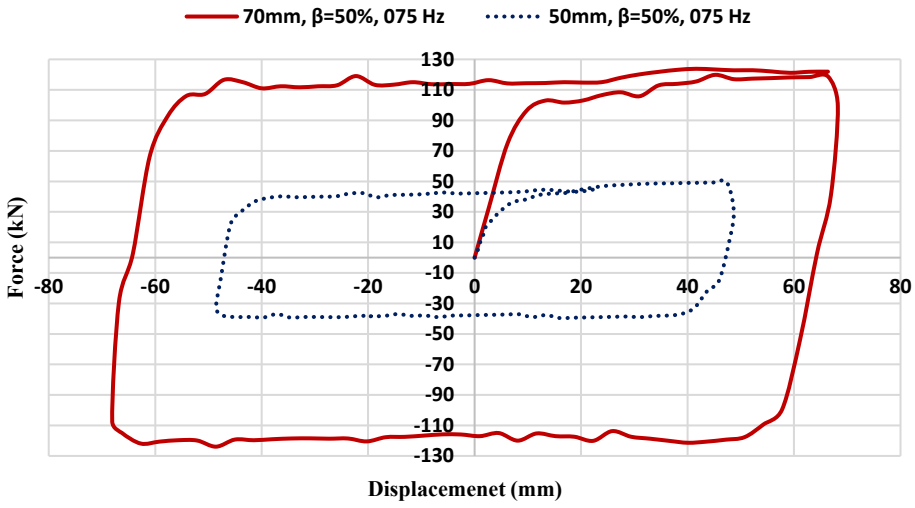

Fig. 32. ABFD hysteresis loop at fully closed valves (β = 100 %).

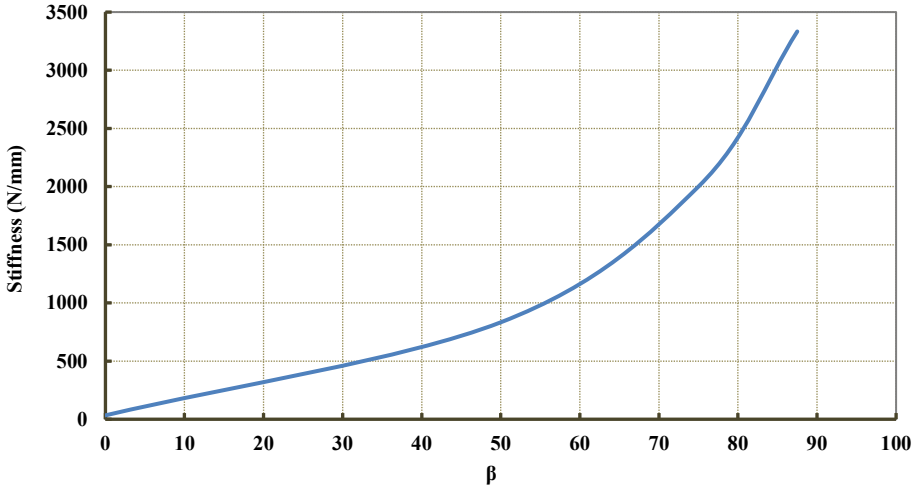

Fig. 33. ABFD stiffness variations according to the different valve positions.

Table 5
Adjustable damping characteristics of the ABFD device.

β (%)	0	50	75	87.5	100
C (N.s/mm)	16.5	816	1666	2203	0
K (N/mm)	33	833	2000	3333	25,000

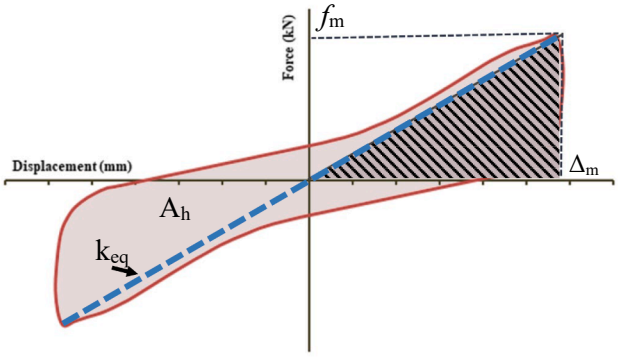

Fig. 34. Parameters to calculate effective damping.

material model of oil and also smooth surface are considered. Also, the friction between hinges and other parts of the device is not fully considered. But in the experimental test, the viscosity of oil may a little change, while surface frictions, hinges frictions, and other parts such as pipe connections may lead to having higher pressure for the fluid during the functioning of the device and accordingly less damping performance in comparison to analytical analysis.

The variation of the damping coefficient according to the β is shown in Fig. 37. In these graphs, the experimental data are compared with the predicted data from the formulated analytical model. This comparison reveals that for valve closing of more than 75 % percent, $\beta \geq 75\%$, the overall behavior of the ABFD device changes from damper to the restrainer. So, the accuracy of the analytical model prediction is desirable for the β values below 75 %. The same pattern can be seen in Fig. 38 for the damping force experimental and numerical data.

4.4. Comparison of ABFD device with similar Restrainer/Damping systems

To validate the superiority of the proposed method, performance of ABFD device has been compared to the Volumetric Compression Restrainer (VCR) device which is implementing in structures as rubber restrainer [7].

The force–displacement curves for VCR devices have been illustrated in Fig. 39-a for rubber cubes with and without holes. The force for the rubber restrainer device can be only change only through adding holes in the rubber tubes (to reduce rubber section area) and also changing size of device and rubber tubes. The hysteresis response of ABFD device in various valve positions also showed in Fig. 39-b. To make proper comparison, the resistant forces for both devices are adjusted to 100kN. As it can be seen in these graphs, performance of VCR device is constant and only able to slightly change the behaviour from restrainer device to damping system (with very low damping) by adding holes in the rubber section. However, performance of ABFD device can be easily change through shifting the valve position to alter action of device from fully restrainer system (β = 100 %) to fully damping device with various damping properties. By consider of both device dimensions to generate resistant force in range of 300kN as benchmark, it is revealed that, the cost of fabrication for both devices are almost same since steel is the main material for building them.

Therefore, through specific design calculation, it is possible to specify dimension of device to generate expected resistant force, however, mostly it is required to change performance of device according to changing applied loads to the structure or altering function and performance level of building. In this case, most of restrainer systems such as rubber restrainer device are not able to accommodate with applied changes and it causes lots of cost and construction work to change all

Table 6
Cyclic Load Frequency Test Results.

Max Displacement (mm)	Frequency (HZ)	Max Damping Load (kN)	Damping Coefficient (N.s/mm)
50	0.5	17	816
50	0.75	23	1540
50	1	50	2750

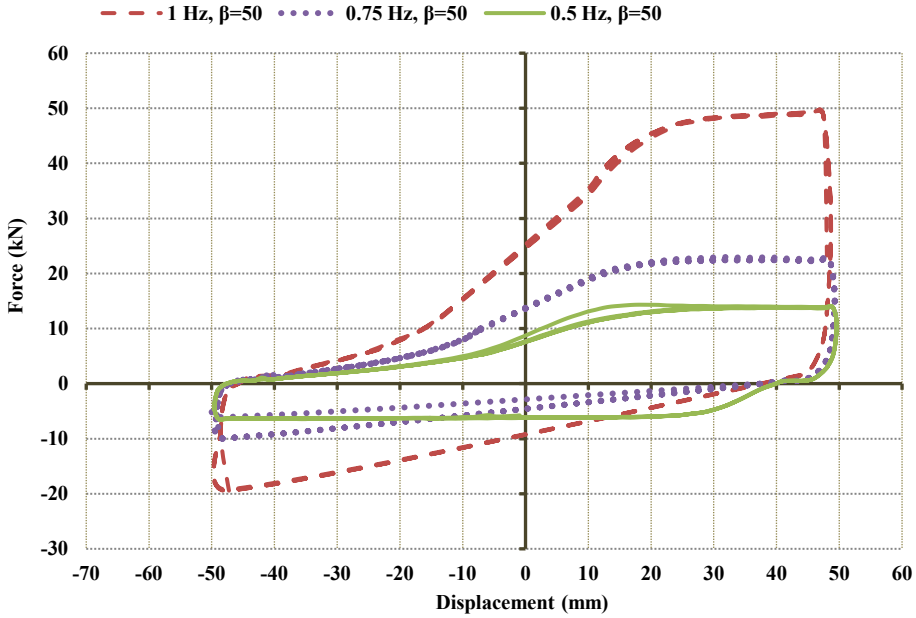

Fig. 35. ABFD stiffness variations according to the different valve positions.

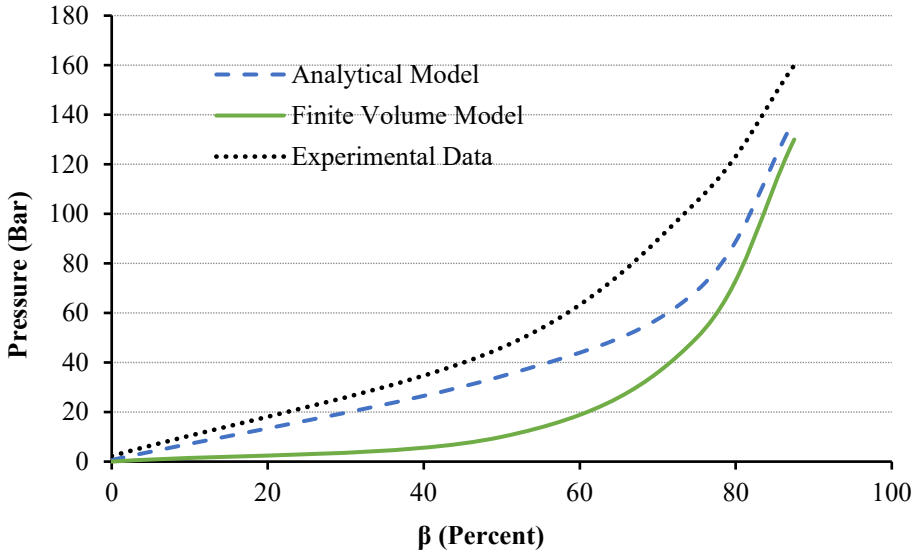

Fig. 36. Pressure Data validation through different approaches.

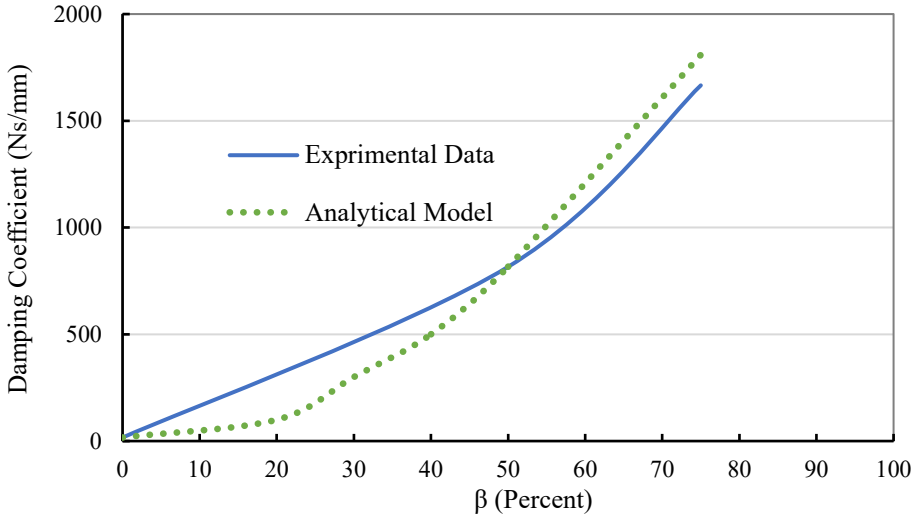

Fig. 37. ABFD Damping coefficient, experimental and numerical data.

devices. However, for ABFD device, only by adjusting control valve, it is possible to adjust action of device according to expected damping/resistant force to diminish effect of imposed excitations.

Therefore, the ABFD device not only can act as a restrainer but also can be regulated to function as a damper device with different capacities by a simple manual control.

Also, as it can be seen in the results, VCR device is able to accommodate a short range of displacements (20 mm to 30 mm), since it is function is depend on hardness of rubber, length of rubber tubes, and holes dimensions, however ABFD device is able to function in very extensive range of movement amplitudes due to its adjustable action to flow oil between two chambers in the cylinder.

5. Development of finite element program for modeling and analysis of the 91/5 overcrossing bridge structure equipped with ABFD device

The 91/5 overcrossing bridge, shown in Fig. 40 (a), located in Orange County in southern California, was considered in this study to implement the ABFD device to the structure of the bridge and evaluate the effect of the damper device on the overall response of bridge subjected to applied loads. The bridge deck is supported at mid-span by a pre-stressed outrigger beam and is furnished with ABFD dampers. A finite element model of the bridge was performed by utilizing the dimensions highlighted in Fig. 40 (b). The bridge's length is considered to be equal to 117 m, and the support beam is located at the mid-span of the bridge [12]. The structure is modeled with different boundary conditions, including a bare structure, two, and four dampers installed between the pier and the deck (Fig. 40 (c)).

The bridge is considered to be constructed from concrete grade C40 with Compressive Strength of 42.5 MPa, Young's modulus of 33.2 GPa, and Poisson's Ratio (ν) of 0.2.

An HS20 traffic load from the ASSHTO standard code has been applied to the bridge which is considered maximum traffic loading of 32 (kN/m) per lane. The traffic load is assumed to travel along the bridge with a max allowable vehicle speed of 65 mile/h based on the US department of transportation, the National Highway Traffic Safety Administration [23], and ASSHTO HS20 (American Association of State Highway and Transportation Officials).

As it is shown in Fig. 41, the bridge is divided into separate sections that are exposed to the weight of the vehicle in a different time step in addition to the weight of the structure. Solid 186 Element has been used

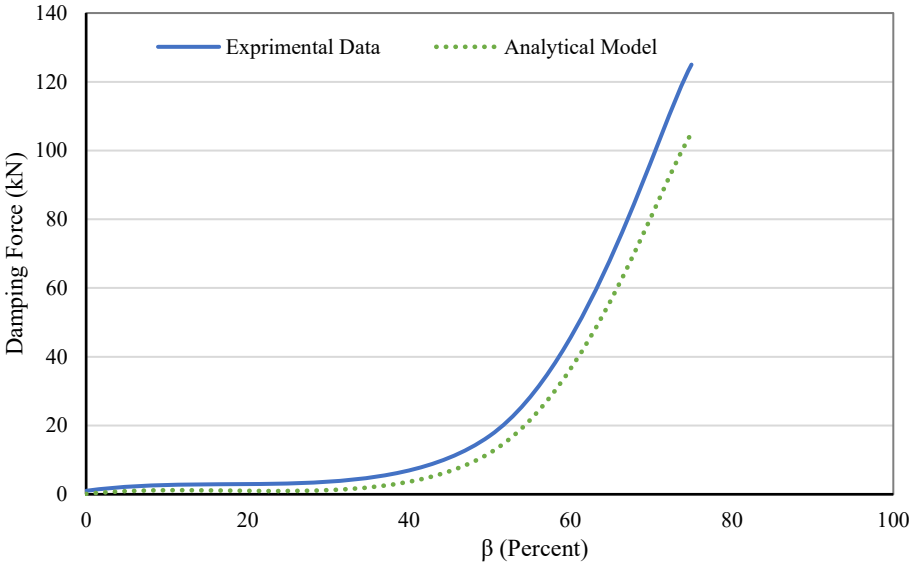

Fig. 38. ABFD Damping force, experimental and numerical data.

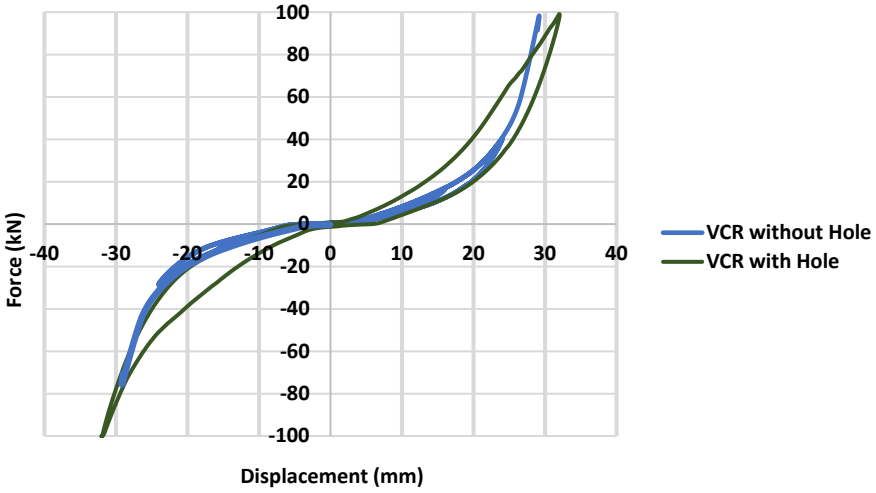

(a): Hysteresis response of VCR device with and without holes

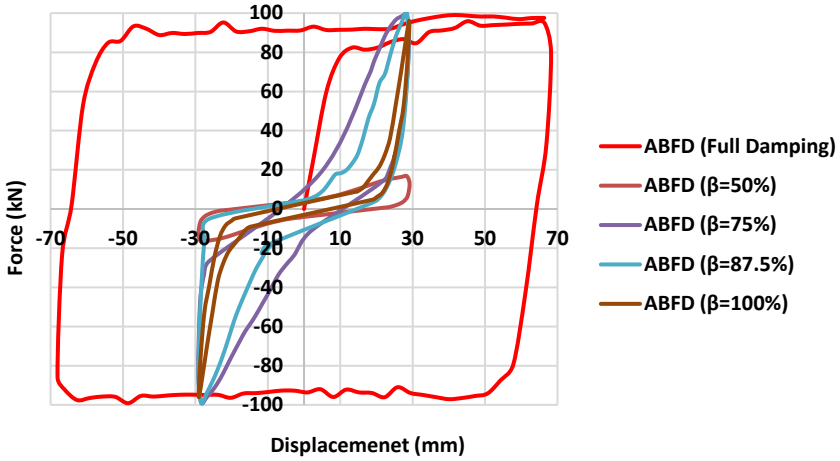

(b): Hysteresis response of ABFD device in various valve positions

Fig. 39. Comparison of performance between Rubber Restrainer Device and ABFD Device.

(a) Finite element model of the bridge

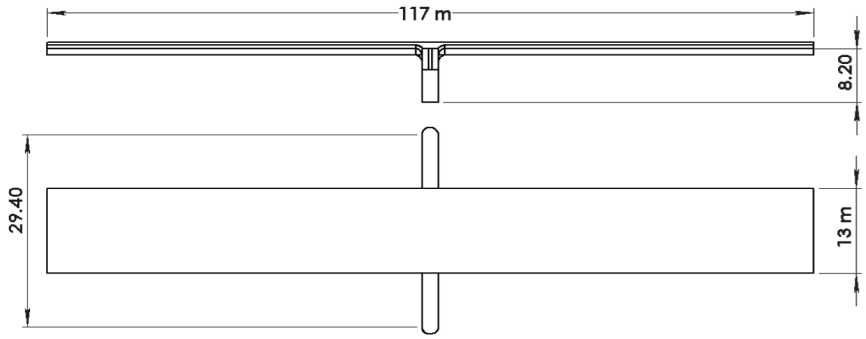

(b) Bridge dimensions and characteristics.

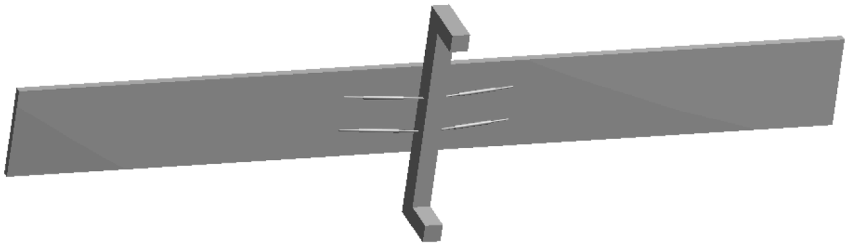

(c)Finite element model of the bridge equipped with four ABFD dampers.

Fig. 40. Finite element model of 91/5 overcrossing in southern California.

to model the concrete sections of the bridge. The force has been applied to one section of the bridge deck at each time step. Mesh independency evaluation has been conducted and the results are shown in the following graphs.

The validation of the finite element model has been done through a comparison of the analysis results with the output of a published paper by Markis and Zhang [33]. They have done a thorough study on the effectiveness of installed fluid dampers in the same bridge (19/5 overcrossing, California).

The Damper has been placed between the bridge deck and the pier of the bridge and has been modeled using the spring-dashpot element refer to Maxwell model.

To conduct the validation, component 164 of the Pacoima Dam Earthquake has been applied to the finite element model and a transient analysis has been done and the drift of the column of the bridge has been calculated and compared. the results show a very good agreement between the finite element model and the results of the former study. The results are demonstrated in Figs. 42 and 43.

To obtain reliable results for the finite element analysis, a precious mesh independency study has been carried out. Figs. 44 and 45 show the effect of element configuration including Hexahydrone and Tetrahydrone elements, on the stress and deflection of the bare bridge structure under traffic loads. Fig. 46 demonstrates that the element size of less than 200 mm provides reliable simulation results for the assumed bridge and loading configuration.

6. Results and discussion

The response of the bare bridge in comparison with a bridge equipped with 2 and 4 dampers while dampers regulated on β from 0 to 75 percent is demonstrated when a 19/5 concrete bridge structure is exposed to the transient force from HS20 ASSHTO traffic loads. The total deformation of the bare bridge and bridge equipped with 2 and 4 dampers is represented in Fig. 47 (a), (b), and (c). The finite element

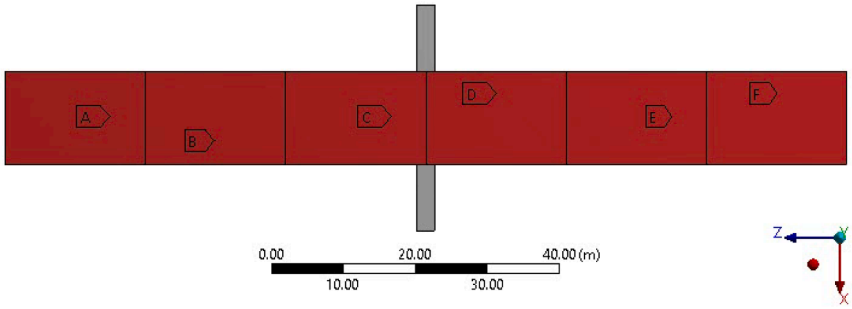

(a) Transient force configuration

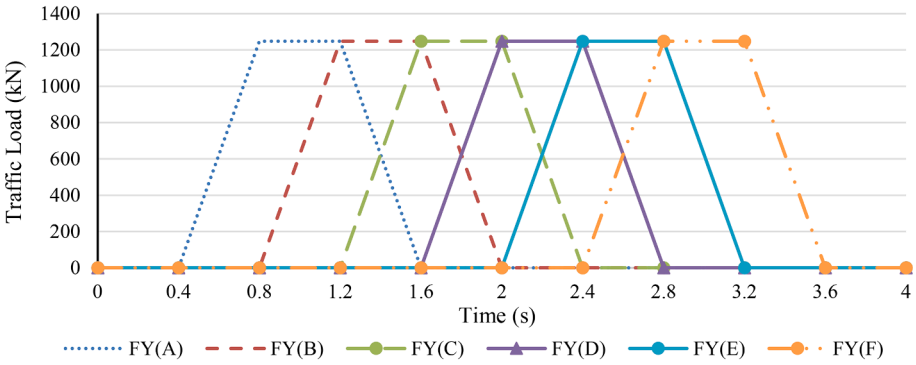

(b) Transient force pattern and amount

Fig. 41. Transient force configuration applied to the bridge.

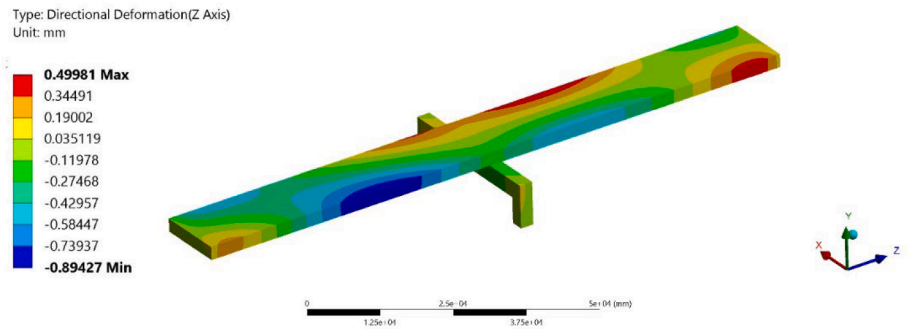

Fig. 42. Deformation result of 91/5 bridge, California subjected to Pacoima Dam Earthquake records (1971 San Fernando, California).

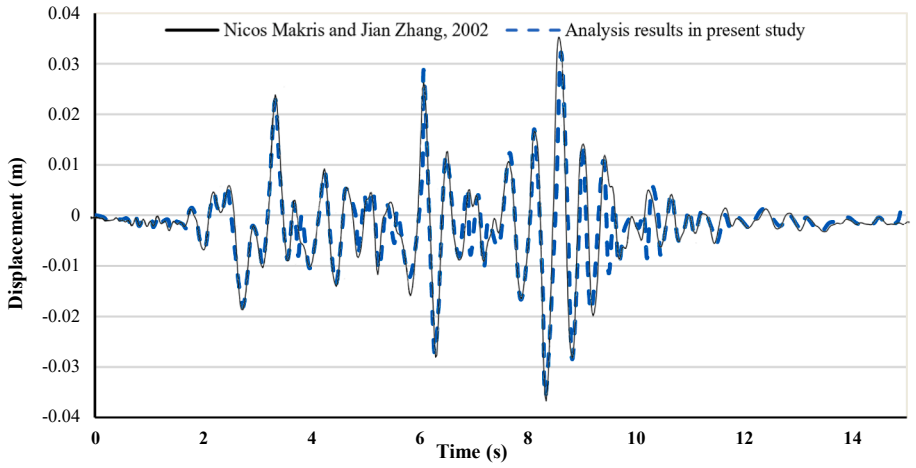

Fig. 43. Drift time histories result for of the north column of 91/5 bridge, California subjected to Pacoima Dam Earthquake record (1971 San Fernando, California).

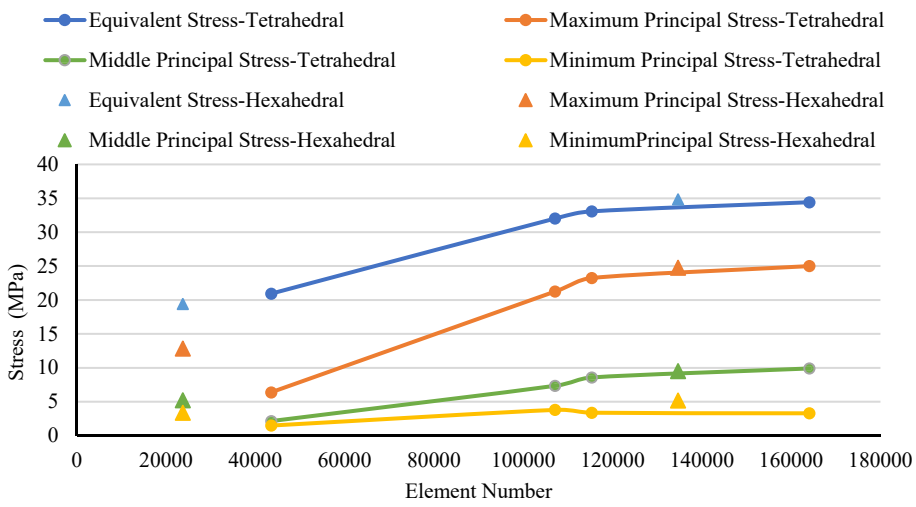

Fig. 44. Mesh independency study, Stress versus element number.

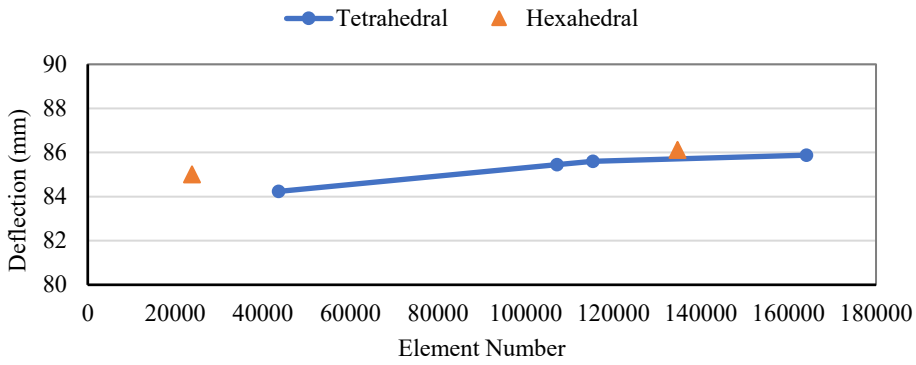

Fig. 45. Mesh independency study, Deflection versus element number.

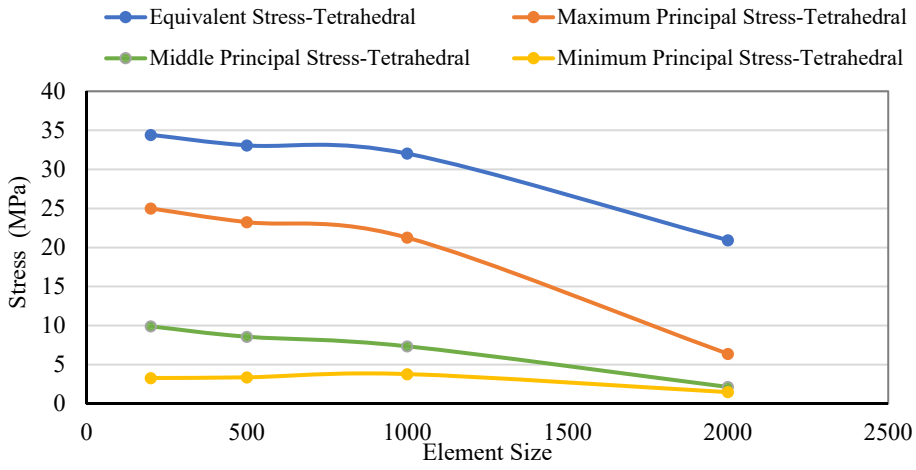

Fig. 46. Mesh independency study, stress versus element size.

analysis of the bridge shows adding 2 ABFD dampers mitigate the total deformation of the bare structure by 18 % (Fig. 46(b)). While an increasing number of dampers to 4 dampers improves the total deformation of the bridge by 29 % (Fig. 47(c)).

The bridge midspan displacement values are charted in Fig. 48 and show implementing two ABFD devices can mitigate the response of the bridge during loading time steps by up to 29 %.

The reaction force of the piers and abutment of the bridge equipped with 2 dampers are calculated and depicted in Figs. 49 and 50, respectively, and show by the mean of 2 sets of ABFD dampers the reaction force at the piers has been decreased up to 12.6 percent and at the abutment, it would be up to 11.3 percent.

For a better understanding of the effectiveness of the damper on mitigating midspan displacement, normalized displacement for structure equipped with 4 dampers is calculated and demonstrated in Fig. 51. To compute the normalized displacement, all the resultant

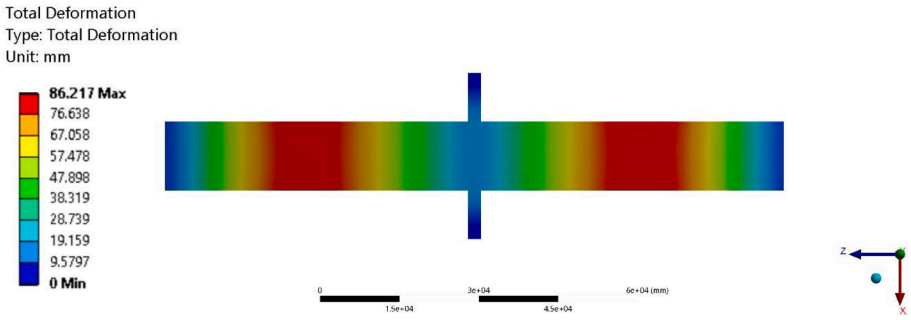

(a) Bare Bridge total deflection subjected to vehicle load

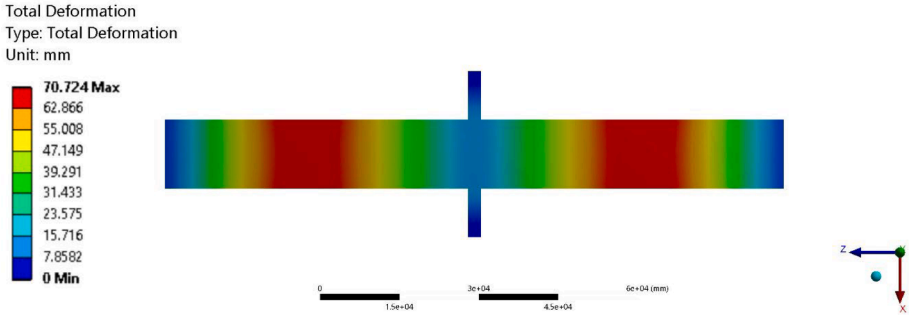

(b) Total deflection of the bridge equipped with 2 dampers, β=50%

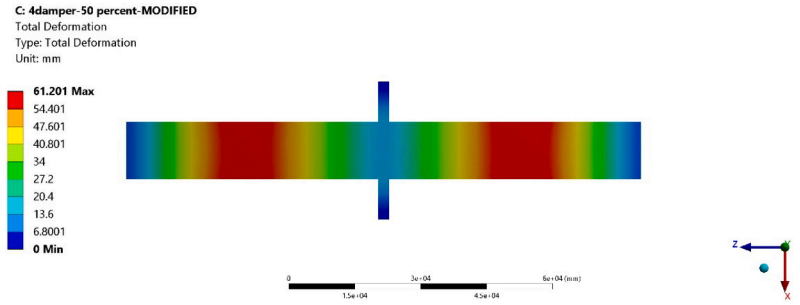

(c) Total deflection of the bridge equipped with 4 dampers, β=50%

Fig. 47. Bridge total deformation after applying 2 and 4 sets of ABFD dampers, β = 50 %.

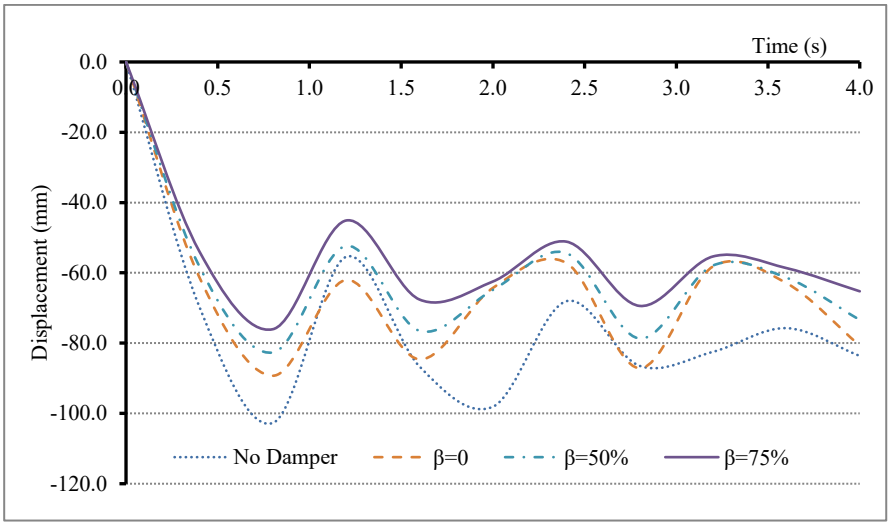

Fig. 48. Midspan displacement of the bridge equipped with two sets of ABFD dampers in comparison with Bare structure.

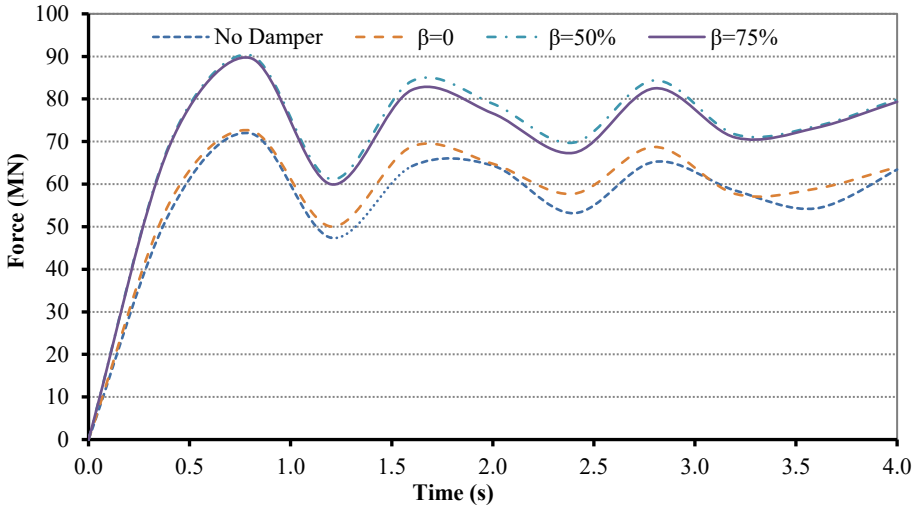

Fig. 49. Piers force reaction reduction after installing 2 ABFD dampers.

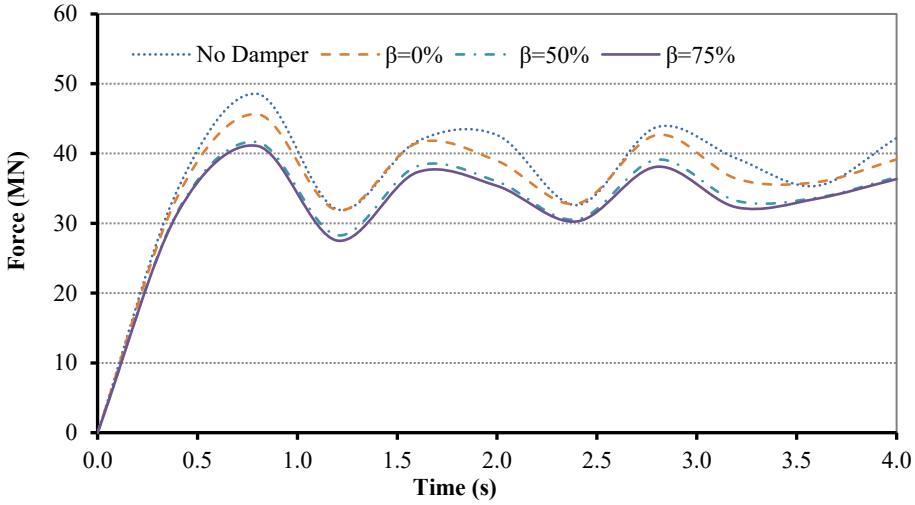

Fig. 50. Abutment force reaction reduction after installing 2 ABFD dampers.

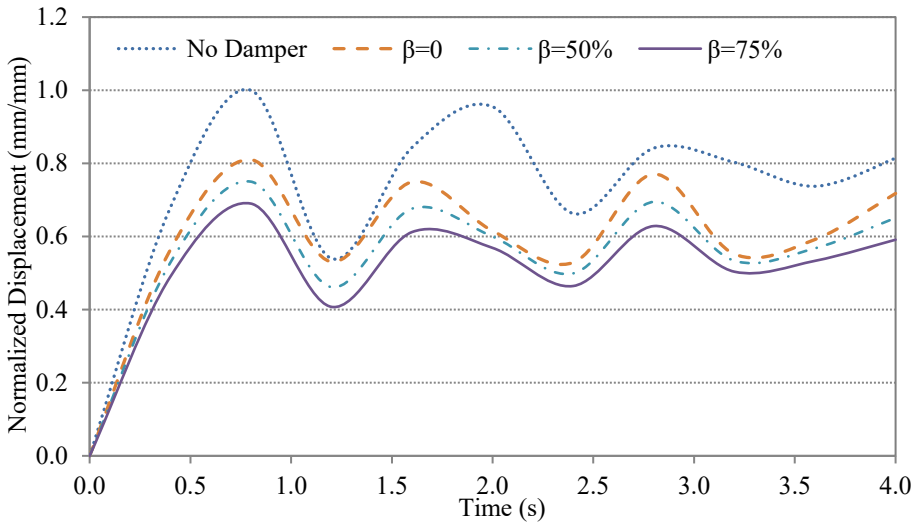

Fig. 51. Normalized midspan displacement before and after using ABFD dampers.

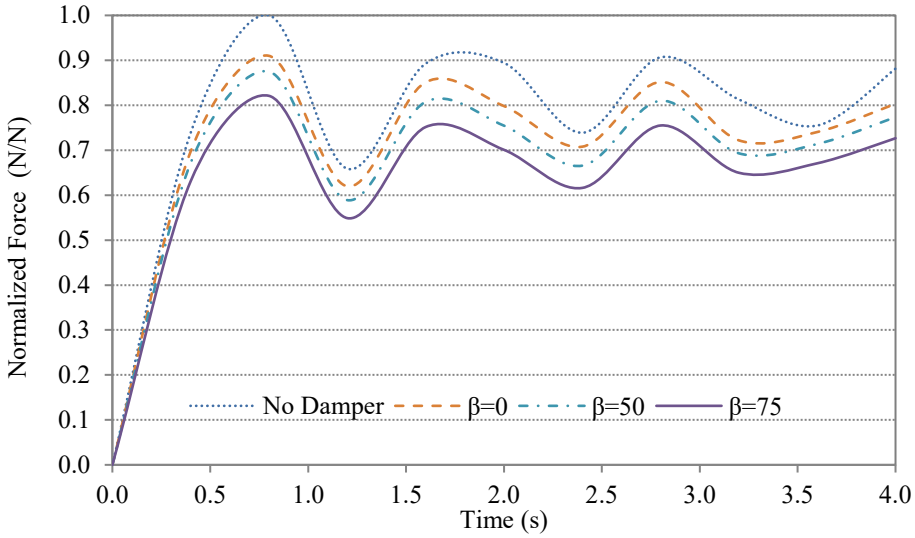

Fig. 52. Normalized pier force reaction before and after using ABFD dampers.

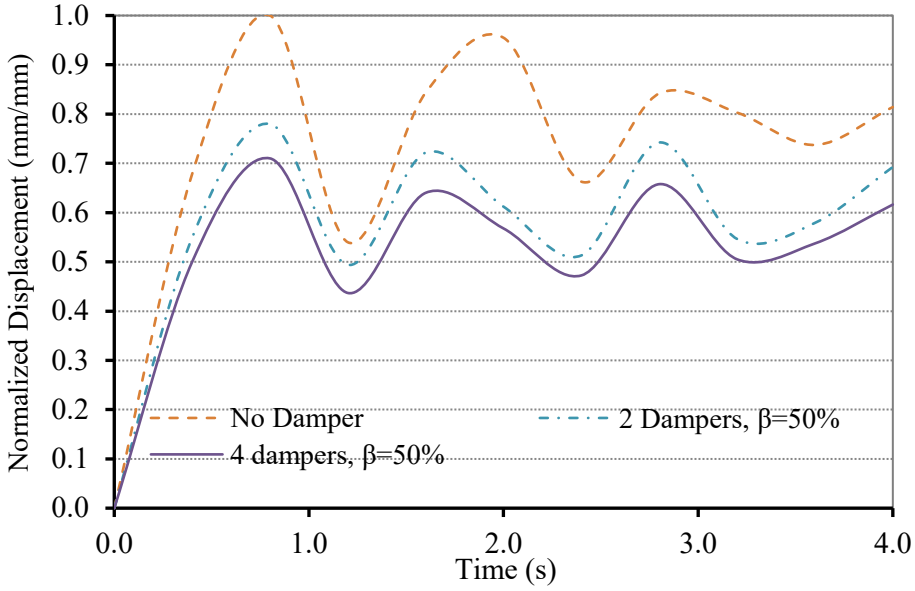

Fig. 53. Bare structure maximum displacement in comparison with equipped

Table 7
The effectiveness of the ABFD device for reducing the bridge structure dynamic response.

	β	Reduction Percentage	
		2 Dampers	4 Dampers
Midspan Displacement	0	15 %	20 %
	50	22 %	29 %
	75	29 %	31 %
Piers Force Reaction	0	6.3 %	9 %
	50	10.4 %	12.5 %
	75	12.6 %	17.9 %
Abutment Force Reaction	0	5.15	6.2 %
	50	9.27 %	12 %
	75	11.3 %	16.2 %

displacements are divided and compared with the maximum midspan displacement of the bare structure. So, normalized displacement is a dimensionless parameter and is clearly showing that when the bridge is equipped with the dampers, midspan displacement is enhanced up to 31 % (Fig. 51).

The same approach for reaction force of the piers of the bridge equipped with 4 dampers is considered. Thus, normalized force is introduced as a dimensionless parameter to make the comparison step clear. This parameter also is computed by dividing all the resultant reaction force data by the maximum reaction force of the bare bridge. The normalized parameter for the reaction force of the pier is illustrated in Fig. 52. This graph demonstrated that by the mean of 4 ABFD dampers the reaction forces in the piers are decreased up to 17.9 percent.

The displacement of the bare structure is compared with the structure equipped with two and four dampers at $\beta = 50$ %, when valves are half-closed, to compare the damper effectiveness in the bridge. The results are depicted in Fig. 53. This graph demonstrates the normalized displacement versus time steps during the traffic load passing over the bridge. In conclusion, the installation of four dampers can reduce the bridge's maximum displacement by up to 31 percent.

The investigated results of the effectiveness of the ABFD device on the bridge structure under applied dynamic loads are summarized in

Table 7. These outcomes show that utilizing the ABFD device as a damper can reduce the overall structure displacement by up to 31 %.

Therefore, additional damping or restrainer system is required to control the large displacement and dissipate bridge vibrations. Based on prior studies available in the literature, the application of viscous damper in the bride has effectively reduced the vibration effect on the bridge under applied catastrophic loads and successfully protects the rubber bearing against excessive displacement by limiting the large displacement .

7. Conclusion

In the current study, a new Adjustable Bypass Fluid Damper (ABFD) is developed to implement in the bridge structures between the pier and deck. This device functions to dissipate dynamic energy from the passing vehicles and increase the operational life of the bridge.

To develop the adjustable damper device, firstly, the desirable maximum and minimum damping characteristics have been defined through the primary design procedure. These maximum and minimum damping parameter forms the operational range of the device and have been determined numerically. Afterward, to develop the adjustable performance of the device within the operational bound, an analytical model has been developed and the performance of the device has been formulated based on the opening state of the flow control valve and the pressure of the fluid flow inside the hydraulic cylinder. A finite volume model also has been developed to evaluate the fluid behavior during the operation and the effect of the flow control valve on the velocity and pressure of the fluid. To validate the numerical results, the prototype of the ABFD device has been fabricated and cyclic incremental displacement and load–frequency tests have been conducted using a dynamic actuator. The results indicate the ABFD device generates damping force and dissipates vibration energy successfully. Also, the results revealed a promising agreement between the data from the finite volume, analytical analysis, and experimental tests.

In the next step, the numerical model for the ABFD device was derived and implemented to develop the finite element code for dynamic analysis of a bridge structure equipped with a supplementary ABFD device. The response of a bridge's bare structure was compared with the structures equipped with two and four dampers. Resultant data show that the adjustable bypass fluid damper is capable to develop a wide range of damping levels between an upper and lower bound, and the response of the structure with no dampers (bare structure) is dramatically improved with the addition of the damper system. Results demonstrate that the maximum displacement of the structure can be reduced by as much as 31 percent, by the use of 4 sets of ABFD damper devices.

According to the obtained results, implementing of the automatic servo valves instead of the manual valves able to provide an automatic real-time control on the bridge vibration which proposed as future study to improve function of the semi-active damper device according to the applied load to effectively dissipate applied vibration.

Declaration of Competing Interest

The authors declare that they have no known competing financial interests or personal relationships that could have appeared to influence the work reported in this paper.

References

[1] Bertolesi E., Buitrago, M., Adam, J.A., and Calderón, P.A., (2021) "Fatigue assessment of steel riveted railway bridges: Full-scale tests and analytical approach, Journal of Constructional Steel Research", Volume 182, July 2021, 106664.

[2] Munson BR, Young DF, Okiishi TH, Huebsch WW. Fundamentals of Fluid Mechanics. Sixth ed. John Wiley & Sons Inc; 2009.

[3] Constantinou MC, Symans MD. Seismic response of structures with supplemental damping. Struct Des Tall Build 1993;2:77–92.

[4] Diudea M, Hodor V, Bălan R, Bara M. Cfd prediction of the flow inside the damper by the use of les model. Bull Transilvania Univ Braşov, Series I: Eng Sci 2013;6.

[6] Gong J, Zhou Z, Liu B. Using the unstructured dynamic mesh to simulate multistore separating from aircraft. Proc Eng 2011;16(2011):572–80.

[7] Hejazi F, Farahpour H, Ayyash N, Chong T. Development of a volumetric compression restrainer for structures subjected to vibration. J Build Eng 2022;46: 2352–7102. https://doi.org/10.1016/j.jobe.2021.103735.

[8] JSSI Manual (2003), Design and Construction Manual for Passively Controlled Buildings, Japan Society of Seismic Isolation (JSSI), First Edition, Tokyo, JAPAN, October (in Japanese, 405 pages).

[9] Jugulkar LM, Singh S, Sawant SM. Fluid flow modeling and experimental investigation on automobile damper. Constr Build Mater 2016;121:760–72.

[10] Konstantinidis D, Makris N, Kelly JM. In-situ condition assessment of seismic fluid dampers: experimental studies and challenges. Meccanica 2019;50(2):323–40.

[11] Li H, Yuan XS, Wu B. Experimental study on structures with semi-active fluid dampers. J Vib Eng 2002;25(1):24–9. in Chinese.

[12] Makris N, Zhang J. Structural Characterization and Seismic Response Analysis of a Highway Overcrossing Equipped with Elastomeric Bearings and Fluid Dampers: A case Study. Berkeley, PEER: Pacific Earthquake Engineering Research Center, College of Engineering University of California; 2002. Report 2002/17.

[13] Maljaars J. (2020) "Evaluation of traffic load models for fatigue verification of European road bridges". Eng Struct 2020;225(15):111326.

[14] Moses F, Schilling CG, Raju KS. Fatigue Evaluation Procedures for Steel Bridges. Washington, D.C.: National Cooperative Highway Research Program; 1987.

[15] Murota, N., and Mori, T., (2020) "An Experimental Study on Scale Effect in Dynamic Shear Properties of High-Damping Rubber Bearings, Front. Built Environ, https://doi.org/10.3389/fbuil.2020.00037.

[16] Nakayama H. Application of Dynamic Mesh Method in CFD to Engineering Designs of Needle-Free Liquid Jet Injector and Diaphragm-less Shock Tube. Quebec, Canada August: Concordia University Montreal; 2013.

[17] Niu J, Ding Y, Shi Y, Li Z. Oil damper with variable stiffness for the seismic mitigation of cable-stayed bridge in transverse direction. Soil Dyn Earthq Eng 2019;125:105719.

[18] Niwa N, Kobori T, Takahashi M, Kurata N, Mizuno T, Midorikawa H. Dynamic loading test and simulation analysis of full-scale semi-active hydraulic damper for structural control. Earthquake Eng Struct Dyn 2000;29:789–812.

[19] Patten W.N., Kuo C.C., He Q. et al., (1994) "Suppression of Vehicle-Induced Bridge Vibration via Hydraulic Semiactive Vibrartion Dampers". Proc. of the 1st World Conf. on Structural Control. Pasadena, CA, FA1–30–38.

[20] Sadeghian, M. A., Yang, J., Wang, X., and Wang, F., (2021) "Novel adaptive tuned viscous inertance damper (ATVID) with adjustable inertance and damping for structural vibration control, Structures, Volume 29, February 2021, Pages 814-822.

[21] Symans MD, Constantinou MC. Seismic testing of a building structure with a seismic-active fluid damper control system. Earthquake Eng Struct Dyn 1997;26 (7):759–77.

[22] Tanaka T, Wook S, Chung L-F, Makii KL, Kushibe A, Kohzu M, et al. Post-characteristics of Formed Zn-22 mass%Al Alloy to Seismic Damper for General Residence. Mater Trans 2009;50(8):2127b–b. https://doi.org/10.2320/matertrans.45.2542.

[23] US department of transportation. National Highway traffic Safety Administration. Tenth ed. Summary of State Speed Laws; 2007.

[24] Wijesundara KK, Nascimbene R, Sullivan TJ. Equivalent viscous damping for steel concentrically braced frame structures. Bull Earthquake Eng 2011;9:1535–58. https://doi.org/10.1007/s10518-011-9272-4.

[25] Xiang N, Goto Y, Obata M, Shahria Alam M. Passive seismic unseating prevention strategies implemented in highway bridges: a state-of-the-art review. Eng Struct 2019;194:77–93.

[26] Yang RL, Zhou XY, Yan WM, et al. Performance evaluation of semiactive structural control using variable dampers. J Vib Shock 2007;26(3):37–41. in Chinese.

[29] Yu Y, Royel S, Li J, Li Y, Ha Q. Magnetorheological elastomer base isolator for earthquake response mitigation on building structures: modeling and second-order sliding mode control. Earthquakes Struct 2016;11(6):943–66.

[30] Yu Y, Hoshyar AN, Li H, Zhang G, Wang W. Nonlinear characterization of magnetorheological elastomer-based smart device for structural seismic mitigation. Int J Smart Nano Mater 2021;12(4):390–428.

[31] Yu Y, Royel S, Li Y, Li J, Yousefi AM, Gu X, et al. Dynamic modelling and control of shear-mode rotational MR damper for mitigating hazard vibration of building structures. Smart Mater Struct 2020;29(11):114006.

[32] Zhang H, Liu X. Investigation of the seismic behaviours of three-dimensional high-rise steel frame structures equipped with oil dampers with variable stiffness. J Constr Steel Res 2021;179:106542.

[33] Zhang J, Makris N. Kinematic response functions and dynamic stiffnesses of bridge embankments. Earthq Eng Struct Dyn 2002;31:1933–66.